

Li-Anne Liew<sup>1</sup>

Mem. ASME

Applied Chemicals and Materials Division,  
National Institute of Standards and Technology,  
325 Broadway, Mail Stop 647,  
Boulder, CO 80305  
e-mail: li-anne.liew@nist.gov

David T. Read

Applied Chemicals and Materials Division,  
National Institute of Standards and Technology,  
325 Broadway, Mail Stop 647,  
Boulder, CO 80305  
e-mail: readdt@gmail.com

May L. Martin

Applied Chemicals and Materials Division,  
National Institute of Standards and Technology,  
325 Broadway, Mail Stop 647,  
Boulder, CO 80305  
e-mail: may.martin@nist.gov

Peter E. Bradley

Applied Chemicals and Materials Division,  
National Institute of Standards and Technology,  
325 Broadway, Mail Stop 647,  
Boulder, CO 80305  
e-mail: peter.bradley@nist.gov

John T. Geaney

U.S. Army Combat Capabilities Development  
Command Armaments Center,  
Picatinny Arsenal, NJ 07806  
e-mail: john.t.geaney.civ@army.mil

# Elastic–Plastic Properties of Mesoscale Electrodeposited LIGA Nickel Alloy Films: Analysis of Measurement Uncertainties

*It is well documented that the microstructure and properties of electrodeposited films, such as lithographie, galvanofornung, abformung (LIGA) Ni and its alloys, are highly sensitive to processing conditions hence the literature shows large discrepancies in mechanical properties, even for similar alloys. Given this expected material variability as well as the experimental challenges with small-scale mechanical testing, measurement uncertainties are needed for property values to be applied appropriately, and yet are uncommon in micro- and mesoscale tensile testing studies. In a separate paper, we reported the elastic–plastic properties of 200  $\mu\text{m}$ -thick freestanding films of LIGA-fabricated nanocrystalline Ni-10%Fe and microcrystalline Ni-10%Co, with specimen gauge widths ranging from 75  $\mu\text{m}$  to 700  $\mu\text{m}$ , and tensile tested at strain rates  $0.001\text{ s}^{-1}$  and  $1\text{ s}^{-1}$ . The loads were applied by commercial miniature and benchtop load frames, and strain was measured by digital image correlation. In this paper, we examine the measurement uncertainties in the ultimate tensile strength, apparent Young's modulus, 0.2% offset yield strength, and strain hardening parameters, and compare them to the standard deviations. For several of these properties, the standard deviation cannot be interpreted as the statistical scatter because the measurement uncertainty was larger. Microplasticity affects the measurement of the Young's modulus, thus we recommended measuring the modulus after specimens have been cyclically loaded. These measurement uncertainty issues might be relevant to similar works on small-scale tensile testing and might help the reader to interpret the discrepancies in literature values of mechanical properties for LIGA and electrodeposited films. [DOI: 10.1115/1.4062106]*

**Keywords:** digital image correlation, elastic–plastic properties, LIGA alloys, measurement uncertainty, mechanical testing, mesoscale, strain rate

## 1 Introduction

**1.1 Lithographie, Galvanofornung, Abformung.** There have been many studies reporting the mechanical properties of electrodeposited nickel films, see, for example, the summaries in Refs. [1] and [2]. A class of free-standing electrodeposited nickel and nickel alloy films are those fabricated through the lithographie, galvanofornung, abformung (LIGA) process [3–6]. LIGA is a photolithography-based, wafer-level microfabrication technique which produces high aspect ratio metal structural components with thicknesses ranging from a few micrometers to around a millimeter, and with thickness-to-width ratios up to 1000:1. LIGA is used to fabricate metal structural parts for applications such as micro-electro-mechanical systems (MEMS) sensors and actuators, microfluidic and micro-optics components, electromechanical structures such as resonators and electrical relays, and mold inserts for micromolding. The most common structural materials made in the LIGA process are Ni and binary alloys of Ni.

Since the LIGA technology was first developed in the late 1980s, there has been much interest in the mechanical properties of these materials due to the wide range of applications, but it has been well documented that the properties and microstructure of electrodeposited metal films are highly sensitive to the processing

parameters such as the plating current density, pH, bath chemistry, bath agitation and temperature, among other factors. For example, Woo and Kim [7] reported that the Young's modulus of electrodeposited Ni, measured by resonance methods, varied from approximately 90–200 GPa due to the plating temperature and current density. They also reported that the measurement uncertainty was 4.2%, indicating that the variation was well correlated to the change in processing parameters. This extreme sensitivity to processing conditions has posed challenges to the commercialization of LIGA technology, and the literature shows a large range of values for the mechanical properties.

Electrodeposited nanocrystalline Ni-Fe alloys have also received much interest in recent years due to their high strength and interesting deformation mechanisms [8–10]. Fabricating nanocrystalline Ni-Fe from the LIGA process (for example, Ref. [10]) enables high aspect ratio metal MEMS devices suitable for more challenging operating environments such as those involving large stresses.

**1.2 Tensile Testing.** Many approaches have been developed to measure the mechanical properties of thin and thick films. These include, but are not limited to, tensile testing, indentation, membrane bulge tests, and cantilever beam bending tests. The diversity of test techniques enables measurements of the properties needed for MEMS device design, simulation and failure prediction, as well as for understanding the fundamental mechanisms of material behavior.

Of the many mechanical test approaches available, the uni-axial tensile test is still considered the “gold standard” because it

<sup>1</sup>Corresponding author.

Manuscript received September 15, 2022; final manuscript received February 17, 2023; published online April 6, 2023. Assoc. Editor: Sudeep Sastry.

This material is declared a work of the U.S. Government and is not subject to copyright protection in the United States. Approved for public release; distribution is unlimited.

produces uniform stress fields and the interpretation of the data is straightforward. Unlike some of the above techniques such as indentation, tensile tests also provide information about the material's behavior to fracture. Given that LIGA fabricated devices often have dimensions in the "mesoscale" (which we define as dimensions ranging from about a millimeter down to tens of micrometers, while dimensions an order of magnitude smaller, we define as the "microscale"), measuring the mechanical properties at the mesoscale is often required to capture size effects. However, tensile testing poses several experimental challenges for specimens at this size scale. One obvious challenge is fabricating multiple test specimens with high reproducibility in dimensions, chemistry, and microstructure. Another set of challenges involves the test itself.

Tensile testing of mesoscale LIGA materials has to date been mostly accomplished by use of benchtop loading apparatuses, including miniature commercial tensile test machines, rather than by use of MEMS actuators, which have limited force capacities. (For a brief review of tensile testing of *microscale* specimens using MEMS actuators, see Ref. [11].) Experimental challenges associated with mesoscale tests include: applying and measuring the forces, gripping and aligning the specimens within the test apparatus, and measuring the strain. For a brief review of the techniques and challenges involved in micro- and mesoscale tensile testing, see Refs. [12] and [13]. For a review that includes other mechanical test methods for thin and thick films, see Refs. [14] and [15].

Strain measurement also poses challenges as specimens are scaled down to the mesoscale and below, as crosshead displacement becomes too inaccurate and traditional extensometry unfeasible. Noncontact laser-based strain measurement methods such as the interferometric strain/displacement gauge method [16–19] have been used in many LIGA tensile testing studies over the past two decades. Another noncontact strain measurement technique that has not been as widely used for small-scale testing is digital image correlation (DIC) [20,21]. DIC allows an abundance of information to be obtained from the tensile test such as the measurements of local strains, full field strains, crack nucleation and growth, all of which are of interest in plasticity and fracture.

**1.3 Measurement Uncertainties in Meso- and Microscale Tensile Testing.** Numerous papers in the literature have reported tensile properties of electrodeposited films and LIGA alloys. The properties are usually reported as a range of values, or as a nominal value with error bars representing the standard deviation. While there have been papers reporting tensile properties of LIGA Ni and NiFe [7,22] as well as on polysilicon and Si [23,24] that included error analysis-derived measurement uncertainties in addition to standard deviations, uncertainty analysis appears to be the exception rather than the norm in the field of micromechanics.

Tensile testing is straightforward in principle but in practice presents experimental challenges, some of which can be significant at small size scales. These challenges necessitate the analysis and quantification of the measurement uncertainties to enable the measured property values to be appropriately interpreted and applied by device designers and reliability engineers.

A knowledge of the measurement uncertainties becomes even more important when the property exhibits a wide range of values or a range that is unknown, as is the case with most electrodeposited films. Unlike the standard deviation, the measurement error is independent of the number of samples and should be an indicator of how accurate or "correct" each individual measurement is. Therefore, without knowing the measurement uncertainty, one cannot know whether the standard deviation can be attributed to inherent material and process variability, as is often assumed. Stephens et al. [25] also noted that the literature values for mechanical properties of LIGA Ni are spread over a wide range, and that the large scatter could be attributed in part to "experimental flaws," or measurement uncertainties, thus making the determination of true material variability uncertain.

Knowledge of the measurement uncertainty is particularly important for the Young's modulus. It has been established in the conventional macroscale testing community that the tensile test is not the most reliable way to obtain the Young's modulus, which is best measured using dynamic methods [26–28]. But in the micromechanics and MEMS communities, the tensile test is frequently used to obtain the Young's modulus. A review of the literature shows over 100% variation in values of Young's modulus for LIGA Ni and its alloys, see, for example, the summaries provided in Refs. [25] and [29–31]. Variability in measured values is usually attributed entirely to the material itself, which may be erroneous if the measurement uncertainties are significant. Therefore, an understanding of the measurement uncertainties may help with interpretation and application of literature values.

**1.4 Objectives.** In Ref. [32], we reported the elastic–plastic properties of two mesoscale LIGA Ni alloys. The alloys were a high-strength nanocrystalline Ni-10%Fe (labeled as "Alpha") alloy, and a micrograined Ni-10%Co alloy (labeled as "C"). Both deposited alloy films had nominal thicknesses of around 200  $\mu\text{m}$ . From tensile tests of 48 specimens, we obtained the values of the two alloys' ultimate tensile strengths (UTS), apparent Young's moduli, 0.2% offset yield strengths, and the strain hardening exponents and strength coefficients. These properties were measured at two strain rates: 0.001  $\text{s}^{-1}$  and 1  $\text{s}^{-1}$ , and at each strain rate there were four geometries of specimens, with gauge widths ranging from 75  $\mu\text{m}$  to 700  $\mu\text{m}$ . Size and rate effects were identified with two-factor analysis of variables. The measurement uncertainties were comparable to or less than the statistical scatter (standard deviation) for the UTS and strain hardening parameters. For the Young's modulus, only the 500 and 700  $\mu\text{m}$ -wide specimens of the Alpha material tested at the quasi-static strain rate had uncertainty at or under 10% and less than the standard deviation. For other material/size/rate combinations, the uncertainties in Young's modulus were much larger—up to 80%—and far exceeded the standard deviations. The uncertainty in the 0.2% offset yield strength exceeded the standard deviation for all specimen categories. For those categories, where the measurement uncertainty exceeded the standard deviation, the standard deviation cannot be interpreted as the property variation range.

In this paper, we describe the computation of the above measurement uncertainties in Ref. [32]. This analysis may be relevant to other studies using similar experimental techniques or similar materials and could aid in interpreting the discrepancies in mechanical properties in the literature for electrodeposited Ni alloys, particularly in the Young's modulus.

(Please note that the scope of this paper does not cover the design of the specimens, the test methods, or the nature of the properties measured. These details have been reported in our earlier work which we cite as appropriate. Please also note that the focus of this paper is on error analysis-based uncertainties. These uncertainties are independent of the number of specimens tested and are separate from statistical variability. Due to limited amount of material and specimens available, we were unable to test more than three specimens per test category, which makes the standard deviation an imperfect metric for the statistical variability. However, since the focus of this paper is not on improving the statistics of the measurements but on the error analysis, we compute the standard deviation only to serve as a comparison to the uncertainties.)

Finally, due to microplasticity in electrodeposited metal films, we agree with the recent proposal by Collins et al. [31] that LIGA MEMS devices undergo cyclic loading before deployment, to stabilize the microstructure and mechanical properties. In this paper, we extend this idea to suggest that the Young's modulus of these materials be measured from specimens that have also undergone cyclic stabilization. This will reduce the standard deviation in the modulus so that the modulus values can be more reliably applied to LIGA MEMS design and simulation.

**Table 1 Test matrix showing the two alloys (Alpha and C), two strain rates, and four specimen geometries: S1 (gauge section 200  $\mu\text{m}$  wide  $\times$  2 mm long); S2 (gauge section 500  $\mu\text{m}$  wide  $\times$  3 mm long); S3 (gauge section 700  $\mu\text{m}$  wide  $\times$  3 mm long); S4 (gauge section 75  $\mu\text{m}$  wide  $\times$  1.2 mm long). Three specimens from each category were tested.**

	Alpha	C
0.001 s <sup>-1</sup>	S1	S1
	S2	S2
	S3	S3
	S4	S4
1 s <sup>-1</sup>	S1	S1
	S2	S2
	S3	S3
	S4	S4

## 2 Specimens and Measured Properties

Our mesoscale specimen designs, tensile test techniques, and measured properties are described in detail in Refs. [32] and [33]. The Alpha alloy was a high strength nanocrystalline Ni-10%Fe alloy, and the C alloy was a more ductile micrograined Ni-10%Co alloy. Table 1 summarizes the combinations of material, specimen geometry, and strain rate in this test campaign. For each of the two materials, there were four specimen geometries, consisting of different gauge widths and lengths. The four specimen designs were designated as: S1 (200  $\mu\text{m}$  gauge width  $\times$  2 mm gauge length), S2 (500  $\mu\text{m}$   $\times$  3 mm), S3 (700  $\mu\text{m}$   $\times$  3 mm), and S4 (75  $\mu\text{m}$   $\times$  1.2 mm). The nominal thickness of all samples was 200  $\mu\text{m}$ . The average measured values of width and thickness, and their standard deviations, were reported in Ref. [32]. The following uncertainty analyses for each property was performed on each specimen, so the uncertainty in each of the fabricated dimensions was factored into the uncertainty values. Then, among the specimens in a particular property/material/size/rate category, the largest uncertainty value was reported in Tables 2 and 3. Note that there currently is no ASTM standard geometry for this size of specimen, and while the designs are based on scaled down

versions of ASTM E8, adaptations to ASTM E8 design had to be made to accommodate physical handling at this size scale, nevertheless, the width-to-thickness ratio of at least 0.78 criterion was met for three of our four designs, as described in our earlier papers [32,33]. Finite element analysis was used to design the geometries, in particular for determining the fillet radii and gauge widths, to ensure there would not be premature strain localization and failure [32,33]. We used two test apparatuses, one for the strain rate of 0.001 s<sup>-1</sup>, and the other for strain rate 1 s<sup>-1</sup>. As described in our earlier works, the specimens were held by pins in clevises to allow for self-alignment during the test and to avoid unintended loading through gripping. All specimens broke near the center of the gauge section. Three specimens of each geometry, in each material, and at each strain rate, were tested, for a total of 48 specimens. Forces were measured with load cells and strain was measured by use of DIC on optical micrographs.

Figure 1 shows a photograph of each specimen geometry, typical engineering stress-strain curves from the tests at 0.001 s<sup>-1</sup>, and typical optical images taken at the time of fracture. In particular, Figs. 1(b) and 1(c) show the contrast between the two materials: the Alpha material has much higher strength and less ductility. In our previous work, we show full-field surface strain maps obtained from DIC, and which show uniform deformation until necking [34], but as with our finite element analysis-based specimen design, a discussion of full field strain mapping of these mesoscale specimens is outside the scope of this paper so we refer the reader to our earlier work for a more detailed discussion of those topics. Tables 2 and 3 summarize the elastic-plastic properties of the two alloys along with their associated measurement uncertainties and relative standard deviations. These data were reported graphically in Ref. [32] and are presented here in tabular form to facilitate the following discussion on the uncertainty analysis. There were typically three specimens in each material/size/rate category. The computation procedures for the uncertainties in UTS and Young's modulus are discussed in Secs. 3 and 4, respectively. The computation procedures for the uncertainty in 0.002 offset yield strength is discussed in Sec. 5 and Appendix A, and for that the strain hardening parameters is in Sec. 6 and Appendix B.

**Table 2 Average values of ultimate tensile strength, apparent Young's modulus, and 0.2% offset yield strength of 200  $\mu\text{m}$ -thick Ni-10%Fe (Alpha) and micrograined Ni-10%Co (C) alloys, with gauge widths of 200  $\mu\text{m}$  (S1), 500  $\mu\text{m}$  (S2), 700  $\mu\text{m}$  (S3), and 75  $\mu\text{m}$  (S4), tested at strain rates of 0.001 s<sup>-1</sup> and 1 s<sup>-1</sup>, and the associated measurement uncertainties and coefficients of variation (CV). From Ref. [32]. There were typically three specimens in each rate/material/size category. The uncertainty in the apparent Young's modulus was calculated at a strain of 5  $\times$  10<sup>-4</sup> mm/mm for the C specimens tested at 1 s<sup>-1</sup>, and at 0.001 mm/mm (chosen for engineering purposes) for all other specimens.**

Strain rate	Material	Size	Ultimate strength			Apparent Young's modulus			Yield strength		
			(MPa)	Uncert. %	CV %	(GPa)	Uncert. %	CV %	(MPa)	Uncert. %	CV %
0.001 s <sup>-1</sup>	Alpha	S1	1949	2	1	147	12	14	1394	12	5
		S2	1948	1	0	141	8	10	1432	8	5
		S3	1930	1	1	147	9	5	1412	9	2
		S4	1837	10	2	139	26	10	1282	29	4
	C	S1	604	3	12	143	26	35	411	26	4
		S2	699	2	8	162	18	13	447	18	9
		S3	695	2	8	156	16	35	437	17	11
		S4	597	10	13	141	73	11	402	41	10
1 s <sup>-1</sup>	Alpha	S1	2034	2	0	123	81	9	1609	22-34	5
		S2	2045	2	1	143	50	20	1619	19-35	6
		S3	2041	1	0	140	83	5	1630	26	1
		S4	2046	6	3	192	126	22	1502	30-43	5
	C	S1	657	3	11	99	75	81	435	22-75	27
		S2	751	2	4	140	67	27	505	31-84	17
		S3	798	2	4	108	69	22	525	46-56	3
		S4	661	13	11	103	63	35	438	45-58	4

**Table 3 Average values of the strain hardening exponent and strength coefficient of 200  $\mu\text{m}$ -thick nanograined Ni-10%Fe (Alpha) and micrograined Ni-10%Co (C) material, with gauge widths of 200  $\mu\text{m}$  (S1), 500  $\mu\text{m}$  (S2), 700  $\mu\text{m}$  (S3), and 75  $\mu\text{m}$  (S4), tested at strain rates of 0.001  $\text{s}^{-1}$  and 1  $\text{s}^{-1}$ , as well as the associated measurement uncertainties and coefficients of variation (CV). From Ref. [32]. There were typically three specimens in each rate/material/size category.**

Strain rate	Material	Size	Strain hardening exponent	Uncert. %	CV %	Strength coefficient (MPa)	Uncert. %	CV %
0.001 $\text{s}^{-1}$	Alpha	S1	0.12	5–7	14	3093	2–4	6
		S2	0.11	4–5	14	3008	2–3	5
		S3	0.11	4–5	3	2954	2	1
		S4	0.10	8–30	60	2839	4–12	23
	C	S1	0.12	5–8	17	931	2–4	18
		S2	0.14	5–8	8	1154	3–5	10
		S3	0.14	5–7	5	1146	3–4	8
		S4	0.12	5–13	17	935	2–7	21
1 $\text{s}^{-1}$	Alpha	S1	0.09	5–8	11	2963	2–4	4
		S2	0.09	3–5	22	3012	1–3	8
		S3	0.09	4	6	2991	2	2
		S4	0.12	9–12	19	3402	4–7	7
	C	S1	0.12	5–8	31	1017	2–4	5
		S2	0.12	2–5	27	1149	1–3	9
		S3	0.13	3–5	7	1265	2–3	8
		S4	0.11	10–28	18	931	5–9	17

In preparation for Secs. 3–7, we mention here that in general, three categories of uncertainty that affect the overall uncertainty in the measured properties are:

- (1) Uncertainty due to the accuracy and precision of the instruments
- (2) Uncertainty due to the repeatability and reproducibility of the measurement techniques
- (3) Uncertainty due to the variability of the specimen material itself

In this study, the uncertainty due to instruments (#1) is small compared to the other two categories. For example, the precision of the load cell read out is absorbed by our load cell calibration resulting in a force uncertainty of 0.5 N (see Appendix of Ref. [33]), compared to the maximum force of 250 N measured for the Alpha S3 specimens. We measure strain as ratios of pixel counts on digital photographs, the uncertainty associated with the photographs is small compared to #2 and #3. Therefore, the uncertainties in our reported values are dominated by the uncertainties in categories #2 and #3.

The uncertainties due to (#1) and (#2) are independent of the number of tests conducted [35]. If the uncertainty of the measurement (#1 and #2) is small, the uncertainty due to material variability (#3) is represented by the standard deviation.

The uncertainty due to specimen-to-specimen variability (#3) is known to be non-negligible for electrodeposited metals such as LIGA alloys, as it has been well documented in the literature that the properties of thin and thick films are highly dependent on processing parameters and can vary significantly between, and even within, fabrication runs.

It appears to be common in the micromechanics and LIGA materials literature to report mechanical properties with the standard deviations as error bars, or without error bars entirely. This practice assumes that #3 dominates the uncertainty. However, as we will show in Secs. 3–6, tensile testing at meso- and microscales can give rise to large measurement errors (#2) associated with the apparatuses and measurement techniques themselves, particularly in the Young's modulus and yield stress.

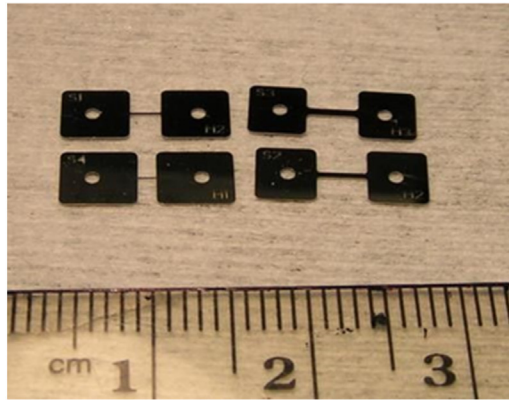
### 3 Measurement Uncertainty in the Ultimate Tensile Strengths

In general, the measurement error is the difference between the true value and the measured value, and the measurement uncertainty is the range that the true value falls within. For the

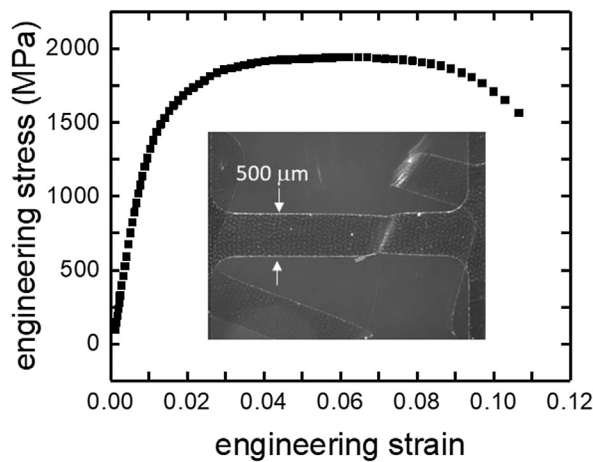
0.001  $\text{s}^{-1}$  tests, we calibrated the 334 N (75 lb) load cell by hanging dead weights in the range of 200–2000 g, in addition to a 11.34 kg weight (25-lb avoirdupois). From three calibration runs, we calculated a force uncertainty of 0.5 N (described in more detail in the Appendix of Ref. [33]). The relative uncertainty in force was calculated as this absolute uncertainty divided by the measured value of the maximum force. Consequently, the relative force uncertainty was under 2% for all but the smallest (S4) specimens, with the C-S4 specimen having the highest relative force uncertainty of 6% due to its low maximum forces (8.4 N on average). For the 1  $\text{s}^{-1}$  tests the load cell was calibrated by the manufacturer and had a reported relative uncertainty in force of 1% of the reading, but from our calibrations, we found that for the force range of 1–20 N (corresponding to the smallest specimens), the force uncertainty was 3%.

Micro-electro-mechanical systems fabrication processes often result in sidewalls that are slightly sloped, resulting in an uncertainty in the gauge width. For each of our specimen designs, the relative uncertainty in the gauge width was calculated as the absolute uncertainty in width divided by the absolute value of the width. The widths were measured with an optical microscope with a 5 $\times$  objective lens and with a resolution of 1540  $\times$  2080 pixels. When calibrated against a standard commercial glass rule, we obtained a conversion factor for our optical microscope of 0.667  $\mu\text{m}/\text{pixel}$ . The absolute uncertainty in width was taken as the difference in the width (measured in pixels) when measured from the top surface versus the bottom surface. We observed that the larger the width, the smaller this difference and thus the more vertical the sidewalls.

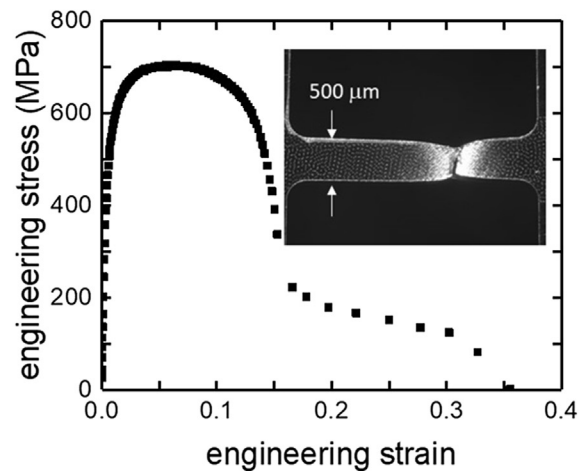
The thickness of each specimen was measured with a digital micrometer at the grip sections so as to avoid damage to the fragile gauge sections. The micrometer had an absolute uncertainty of 0.002 mm. The thickness was measured twice per specimen, once on each grip section, and averaged, and it was assumed that this value is representative of the thickness of the gauge section. The relative uncertainty in the thickness was then calculated as the absolute uncertainty (0.002 mm) divided by the absolute value of the measured thickness. The relative uncertainties in width and thickness were then added in quadrature to obtain the relative uncertainty in cross-sectional area. The relative uncertainties in cross-sectional area and force were then added in quadrature to obtain the relative uncertainty in the UTS. The results are summarized in Tables 4 and 5.



(a)



(b)



(c)

**Fig. 1** (a) Photograph of mesoscale LIGA specimens of each geometry, beside a centimeter ruler [32]. (b) Engineering stress–strain curve of an Alpha (Ni-10%Fe) specimen of the S3 geometry, tested at  $0.001 \text{ s}^{-1}$ , and optical microscope image of the specimen as it fractures. The recoil of the specimen, which is shown within the camera’s exposure time of 162 ms, shows the abruptness of the fracture. (c) Engineering stress–strain curve of a C (Ni-10%Co) specimen of the S3 geometry, tested at  $0.001 \text{ s}^{-1}$ , and an optical microscope image of the specimen just before fracture, showing lower strength but higher ductility compared to the Alpha material.

The above tables show that the uncertainty in the UTS is under 3% for all but the smallest (S4) specimens, being higher in the C material. This trend is expected, because the error is dominated by the uncertainty in the gauge width—stemming from the slightly sloped fabricated sidewalls—since the calculation of stress assumes a rectangular (or in the case of S1, a square) cross section. The uncertainty thus depends on the specimen fabrication process. The Alpha specimens tended to have straighter sidewalls than the C specimens. In addition, the greater the designed width, the straighter the sidewalls. For example, among the specimens tested at  $0.001 \text{ s}^{-1}$ , the relative uncertainty in width for the Alpha-S3 (largest width) was only 1%, while for the Alpha-S4 (smallest) specimens it was 10%. The cross-sectional area could be recalculated as a trapezoid; however, given that this led to less than 1% difference for most of the specimens, we chose to treat it as rectangular and quantify the uncertainty in the width.

Similarly, for the C material, the relative uncertainty in width for the largest (S3) geometry was 2% whereas for the smallest (S4) design it was 7%. The errors in width for these S4/S3 specimens is similar in the higher-rate ( $1 \text{ s}^{-1}$ ) tests as all the specimens came from the same fabrication batches and were randomly assigned to the two strain rates. Since the smallest (S4) C specimens had the largest uncertainty and variability (standard deviation) in width, it is a coincidence that the UTS error for the C-S4 at the higher strain rate was larger compared to C-S4 at the

lower strain rate; it is a result of the specimens randomly selected for the higher strain rate test having a greater range in their widths. Overall, the uncertainty in gauge width dominated the uncertainty in UTS for both alloys, and this uncertainty was due to the sidewalls being sloped to differing degrees while approximated as straight. Table 6 compares the final uncertainties in the UTS due to measurement uncertainty (from Tables 4 and 5 above) versus the standard deviation.

As shown in Table 6, if the smallest (S4) specimens are excluded, the magnitude of the uncertainties in UTS are equivalent to or less than the standard deviations. But with the S4 specimens included, the measurement errors are equivalent to or exceed the standard deviation. This suggests that specimen-to-specimen variability in UTS was too small to be detected in the smallest (S4) specimens due to the limits of the specimen fabrication process, but was sufficiently detected for the S1, S2, and S3 specimens.

#### 4 Measurement Uncertainty in the Apparent Young’s Modulus

In the conventional macroscale mechanical testing community, it has been established that the Young’s modulus is the least reliable property obtained from a tensile test and is best measured

**Table 4 Measurement uncertainty in the UTS, for both material types, by specimen geometry, at strain rate  $0.001 \text{ s}^{-1}$**

Strain rate	$0.001 \text{ s}^{-1}$			
Specimen type	S4	S1	S2	S3
Material	Relative uncertainty in UTS (%)			
Alpha	10	2	1	1
C	10	3	2	2

**Table 5 Measurement uncertainty in the UTS, for both material types, by specimen geometry, at strain rate  $1 \text{ s}^{-1}$**

Strain rate	$1 \text{ s}^{-1}$			
Specimen type	S4	S1	S2	S3
Material	Relative uncertainty in UTS (%)			
Alpha	6	2	2	1
C	13	3	2	2

using resonance or other dynamic methods [26,27]. For microscale testing of Ni, Woo and Kim [7] measured the Young’s modulus of Ni films by electroplating the Ni onto atomic force microscope cantilevers and measuring the resultant change in the atomic force microscope cantilevers’ frequencies and reported a measurement uncertainty of 4.2%. Fritz et al. [36] measured the Young’s modulus of Ni films as a function of plating current density using three different methods: laser acoustic method, micro-indentation, and electrostatic actuation of microfabricated cantilever beams. For many if not most studies on MEMS materials and micro-fabricated specimens, various static methods are often used, such as indentation and static cantilever beam bending (e.g., see Ref. [25]), but each technique also presents challenges. For example, a disadvantage of beam bending methods is that the stress field is nonuniform, and for electrodeposited metals there may also be local plasticity at the surface of maximum stress.

But despite the ubiquity of MEMS mechanical resonators and the large knowledge base supporting their design, fabrication and testing, the Young’s modulus is nevertheless often determined from uni-axial tension tests in the micromechanics and MEMS materials communities, which motivates the discussion in this section.

Note from Table 2 that for strain rate  $0.001 \text{ s}^{-1}$ , the uncertainty in Young’s modulus exceeded the standard deviation in 4 out of 8 material/size categories. At strain rate  $1 \text{ s}^{-1}$ , this was the case for all material/size categories. When the measurement uncertainty exceeds the standard deviation, the latter can no longer be interpreted as the material variability. Thus, the only categories where we could detect the variability in the modulus were Alpha-

S1, Alpha-S2, C-S1, and C-S3, when these specimens were tested at the quasi-static strain rate.

As we show in this section, the uncertainty in the apparent Young’s modulus is dominated by the uncertainty in strain, as the low strains of the linear elastic region correspond to very small relative displacements that are challenging to directly measure accurately. We now discuss how the uncertainties in apparent Young’s modulus were calculated for each material/rate/size category.

**4.1 Computation of the Measurement Uncertainty in Young’s Modulus.**

Several of the C specimens did not have well-defined linear elastic regions. We therefore selected the specimens that had the “best behaved” stress–strain curves for further error analysis (the stress–strain curves can be found in the Appendix of Ref. [33]). When considering this subset of specimens, the average values of apparent Young’s modulus and the relative standard deviations for the C material are as shown in Table 7. All of the Alpha specimens were used in the error analysis.

The uncertainty in apparent Young’s modulus was calculated by adding in quadrature the uncertainties in the engineering stress and the engineering strain, at a nominal strain value. For the Alpha specimens at  $0.001 \text{ s}^{-1}$ , we chose a nominal strain of  $0.001 \text{ mm/mm}$  (corresponding to the “high strain” region since many Alpha specimens exhibited two linear regions due to microplasticity, as discussed in Refs. [32] and [33]) and for the C specimens we chose the nominal strain to be  $0.0005 \text{ mm/mm}$  due to most of the C specimens having shorter linear regions on their stress–strain curves. For the  $1 \text{ s}^{-1}$  tests, a nominal strain of  $0.001 \text{ mm/mm}$  was chosen for all specimens due to the lower resolution of images from the high-speed camera that made smaller strains difficult to determine.

*4.1.1 Calculation of the Uncertainty in Strain.* Since engineering strain is defined as the change in length or “ $du$ ” divided by the initial gauge length “ $L$ ,” the relative error in the strain is calculated by adding the relative errors in  $du$  and  $L$  in quadrature. Both  $du$  and  $L$  were measured in pixels (from the DIC), where the entire gauge length (as opposed to just a section) was imaged to obtain the engineering stress–strain curves. The relative error in  $du$  is the absolute uncertainty in  $du$  divided by the nominal values of  $du$  at the appropriate strains. We now describe in detail the calculation of these individual quantities.

The absolute uncertainty in  $du$  is taken as  $0.2 \text{ pixels}$  for our DIC methods. This corresponds to  $0.28 \text{ }\mu\text{m}$  for the low rate test images, and  $2 \text{ }\mu\text{m}$  for the higher rate test images. This value is a conservative estimate which we originally derived for tensile tests using cameras and microscopes similar to those used in the present  $0.001 \text{ s}^{-1}$  tests and is similar to the value reported by several other researchers who also used DIC to measure strains in micro- and nanoscale specimens [23,37]. Note that Banks-Sills et al. [24] recently reported tensile test results from silicon specimens that were an order of magnitude smaller than our LIGA specimens. They used commercial DIC software to analyze optical micrographs of selected regions of the silicon gauge sections and calculated their uncertainty in the Young’s modulus to be 4%. This small uncertainty stemmed from their absolute uncertainty in  $du$  being only  $0.005\text{--}0.01 \text{ pixels}$ . In addition, whereas we

**Table 6 Summary of the uncertainty in the UTS due to measurement uncertainty versus standard deviation, for both material types and strain rates, averaged over all specimen designs**

Measurement uncertainty and statistical variation in ultimate tensile strength				
	Strain rate $0.001 \text{ s}^{-1}$		Strain rate $1 \text{ s}^{-1}$	
	Uncertainty	Relative standard deviation	Uncertainty	Relative standard deviation
Alpha	<10% (without S4, <2%)	2%	<10% (without S4, <2%)	2%
C	<10% (without S4, <3%)	12%	<13% (without S4, <3%)	12%

**Table 7 Apparent Young’s modulus for the C specimens averaged over all geometries, when considering only the subset of specimens with the best behaved stress–strain curves (12 and three specimens at strain rates  $0.001\text{ s}^{-1}$  and  $1\text{ s}^{-1}$ , respectively) [33]**

Strain rate	Average apparent Young’s modulus (GPa)	Standard deviation (GPa)	Coefficient of variation (%)
$0.001\text{ s}^{-1}$	156	35	22
$1\text{ s}^{-1}$	109	25	23

measured the engineering strain along the full gauge length due to the plasticity of electrodeposited films, Banks-Sills et al. only used portions of their gauge sections for the strain measurement of the silicon since the latter is brittle.

Calculating the relative error in  $L$  is more straightforward; it is similar to calculating the relative error in the gauge width, except that here it is applied to the imaging apparatuses used in the tensile tests. The absolute uncertainty in  $L$  was taken as 40 pixels, as this was the size of the DIC subregion used in our custom DIC program.

The relative errors in both  $du$  and  $L$  are higher for the  $1\text{ s}^{-1}$  tests than for the  $0.001\text{ s}^{-1}$  tests. The  $1\text{ s}^{-1}$  tests used a high-speed camera, which had lower resolution and thus fewer pixels. For example, we calculated that for the Alpha-S1 specimen category, the relative uncertainty in  $du$  is 10% for the low-rate test but 80% for the higher rate test [33].

**4.1.2 Calculation of the Uncertainty in Stress.** The uncertainty in the stress is calculated similarly to that in the UTS, except that here the forces used are those corresponding to the appropriate nominal strains. Finally, the corresponding relative uncertainties in stress and strain are added in quadrature to obtain the relative uncertainties in the modulus for each material/size/rate category.

**4.1.3 Results of the Calculation of the Young’s Modulus Uncertainty.** Table 8 and Appendix H in Ref. [33] show the contributions of the uncertainties in force,  $L$ , width, and  $du$ , to the total measurement uncertainty in the Young’s modulus for each material/size/rate category. Figure 2 shows a summary of the Young’s modulus uncertainty for the quasi-static test. The calculated uncertainties are for one standard deviation or 68% confidence level. For two standard deviations or 95% confidence

level, multiply these values by two. Figure 3 shows the contributions of the individual experimental factors to the total uncertainty for the two extreme specimen categories (in terms of forces and displacements): Alpha-S3 and C-S4.

From Fig. 2 above, note that for the Alpha-S2 and Alpha-S3 categories the measurement uncertainty is under 10%, which we consider to be an acceptable level. For all other categories, however, the uncertainty is much higher. This is due to the smaller displacements in the other categories (because Alpha S1 and S4 have shorter gauge lengths, while all the C specimens were analyzed at a smaller nominal strain of  $5 \times 10^{-4}$  compared to the  $0.001$  nominal strain for the Alpha specimens.)

Figure 3 shows that the uncertainty in strain dominates the overall uncertainty in modulus, for the larger specimens. For the smallest (S4) specimens, the relative uncertainty in force is comparable to that for the strain, due to the very low stresses in the linear elastic region of the smallest specimens. This could be mitigated to some degree by use of a smaller loadcell.

Figure 4 shows the measurement uncertainties in the higher-rate test. As with the quasi-static tests, the measurement uncertainty in Young’s modulus is dominated by the error in  $du$ , which is higher for the  $1\text{ s}^{-1}$  tests because of the poorer resolution of the high-speed camera. Strain uncertainty is often increased when testing at higher strain rates, as most high-speed cameras have lower image resolution than their lower speed counterparts. Thus, the uncertainty in the modulus is higher across all specimen sizes, for the higher strain rate tests.

Figure 4 also shows that for the  $1\text{ s}^{-1}$  tests the uncertainty is usually higher for the Alpha material. This is due to a systematic shift in our experiments: the magnification of the images in this test setup is not constant but is determined by the distance between the high-speed camera and the specimen. During the period of Alpha testing the camera had been positioned further away from the specimens than during the period of C testing, thus the Alpha images had lower magnification and thus fewer pixels in the gauge section, which led to a greater relative uncertainty in the strains. Figure 5 shows the contributions to the uncertainty in the modulus for the  $1\text{ s}^{-1}$  tests.

**4.1.4 Strain Rate  $1\text{ s}^{-1}$  Tests: Contribution of Experimental Apparatus Synchronization to the Young’s Modulus Uncertainty.** The  $1\text{ s}^{-1}$  tests of the C material had an additional source of measurement uncertainty due to the synchronization between the force data and the acquired images. As described in Refs. [32] and [33], in our  $1\text{ s}^{-1}$  test setup the force data and images were acquired on separate computers and had to be manually

**Table 8 Contributions to the uncertainty in apparent Young’s modulus for each material/size/rate category**

Strain rate	Relative uncertainty (%)							
			Width	Thickness	Area	Force	Length	$du$
$0.001\text{ s}^{-1}$	Alpha	S1	1	0	1	6	3	10
		S2	1	0	1	3	2	8
		S3	1	0	1	1	2	9
		S4	9	0	9	20	5	15
	C	S1	2	0	2	7	3	25
		S2	2	0	2	4	2	17
		S3	2	0	2	2	2	16
		S4	7	0	7	58	5	44
$1\text{ s}^{-1}$	Alpha	S1	2	0	2	1	7	81
		S2	1	0	1	1	5	50
		S3	1	0	1	1	6	82
		S4	6	0	6	3	6	126
	C	S1	3	0	3	1	8	74
		S2	1	0	1	1	5	67
		S3	1	0	1	1	5	69
		S4	13	0	13	3	6	61

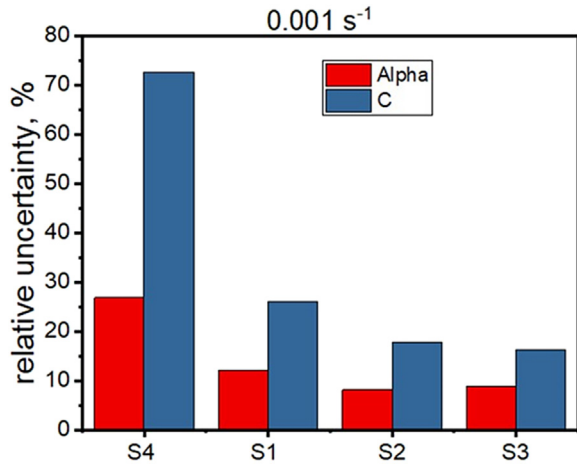


Fig. 2 Calculated measurement uncertainties for the apparent Young's modulus (at a strain of 0.001 for Alpha and  $5 \times 10^{-4}$  for C) in the quasi-static tests, for each specimen size. The average values of the Young's modulus are in Table 1. The gauge widths are:  $75 \mu\text{m}$  (S4),  $200 \mu\text{m}$  (S1),  $500 \mu\text{m}$  (S2), and  $700 \mu\text{m}$  (S3).

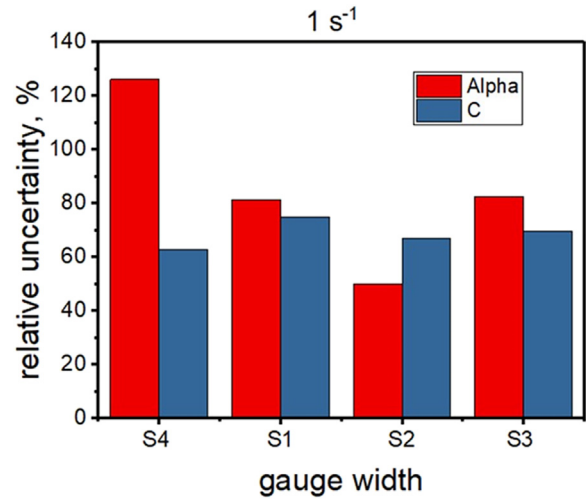


Fig. 4 Measurement uncertainty in apparent Young's modulus (at a nominal strain of 0.001) for the  $1 \text{ s}^{-1}$  test. The gauge widths are:  $75 \mu\text{m}$  (S4),  $200 \mu\text{m}$  (S1),  $500 \mu\text{m}$  (S2), and  $700 \mu\text{m}$  (S3).

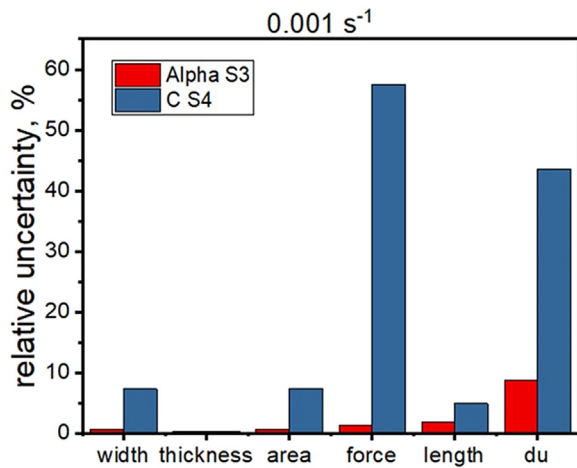


Fig. 3 Contributions to the measurement uncertainty in apparent Young's modulus (at a strain of 0.001 for Alpha and  $5 \times 10^{-4}$  for C) for the quasi-static tests, for the two extreme force–displacement categories of Alpha-S3 and C-S4. The contributions for the other material/geometry categories fall in between these two cases.

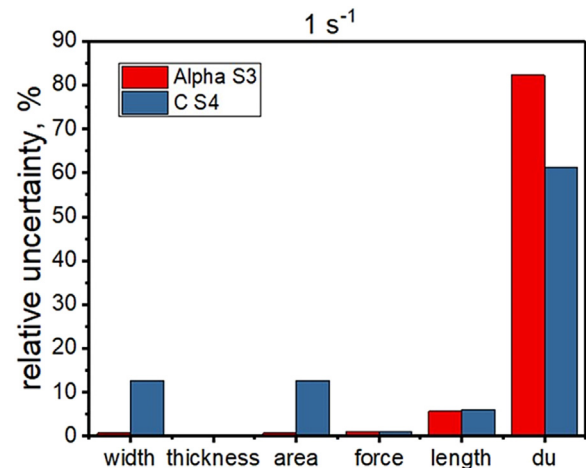


Fig. 5 Contributions to the measurement error in apparent Young's modulus (at a nominal strain of 0.001) for the medium-rate tests, for the opposite extreme force–displacement categories of Alpha-S3 and C-S4. The contributions for the other material/geometry categories fall in between these two cases.

synchronized during the postprocessing of the data. We used the specimen's fracture as the time of synchronization because the fracture event can be clearly distinguished as a sudden drop in the force as well as by the specimen coming apart into two pieces in the images. With the more brittle Alpha specimens, this technique worked well, as the fracture is clearly identified in the images. For the more ductile C specimens, however, there is some difficulty in identifying exactly when (which image) the specimen comes apart. An example is shown for one specimen in Fig. 6, where the fracture could have occurred in any of these images. Since in our  $1 \text{ s}^{-1}$  test analysis procedure the force data and strains are synchronized with respect to the time of fracture, an uncertainty in choosing the correct image therefore leads to an uncertainty in the synchronization. The forces and strains themselves do not change if a different image is chosen, but which forces correspond with which strains (and therefore the slope of the curve) does. Figure 7 illustrates how the resultant stress–strain curve differs significantly in the linear region when the synchronization is varied by seven images.

The uncertainty in the strain due to the uncertainty in synchronization may be computed as follows: For a given C

specimen in the  $1 \text{ s}^{-1}$  test, the range of ambiguous images corresponding to fracture is identified, and a nominal image among these is selected for the initial synchronization and constructing the initial stress–strain curve. From the curve a strain value of 0.001 is selected, and the image it corresponds to is identified. The number of ambiguous images is then counted backward (or forward) from this image, and the respective strain at that end image is calculated. The difference in value between the nominal strain and the strain at the end image is taken as the absolute uncertainty in strain due to the synchronization. For the specimen shown in Figs. 6 and 7, this uncertainty due to synchronization was 8% when the absolute uncertainty was normalized with respect to a strain value at the end of the linear region where the material is no longer linear elastic. This uncertainty due to synchronization can then be added in quadrature to the measurement uncertainty in strain and the uncertainty in stress, to calculate an updated value of uncertainty in the apparent Young's modulus. We did not, however, include this addition in the uncertainty values in Table 2.

This synchronization issue is only present in our  $1 \text{ s}^{-1}$  tests of the C material. The Alpha material, as shown in Fig. 1(b),

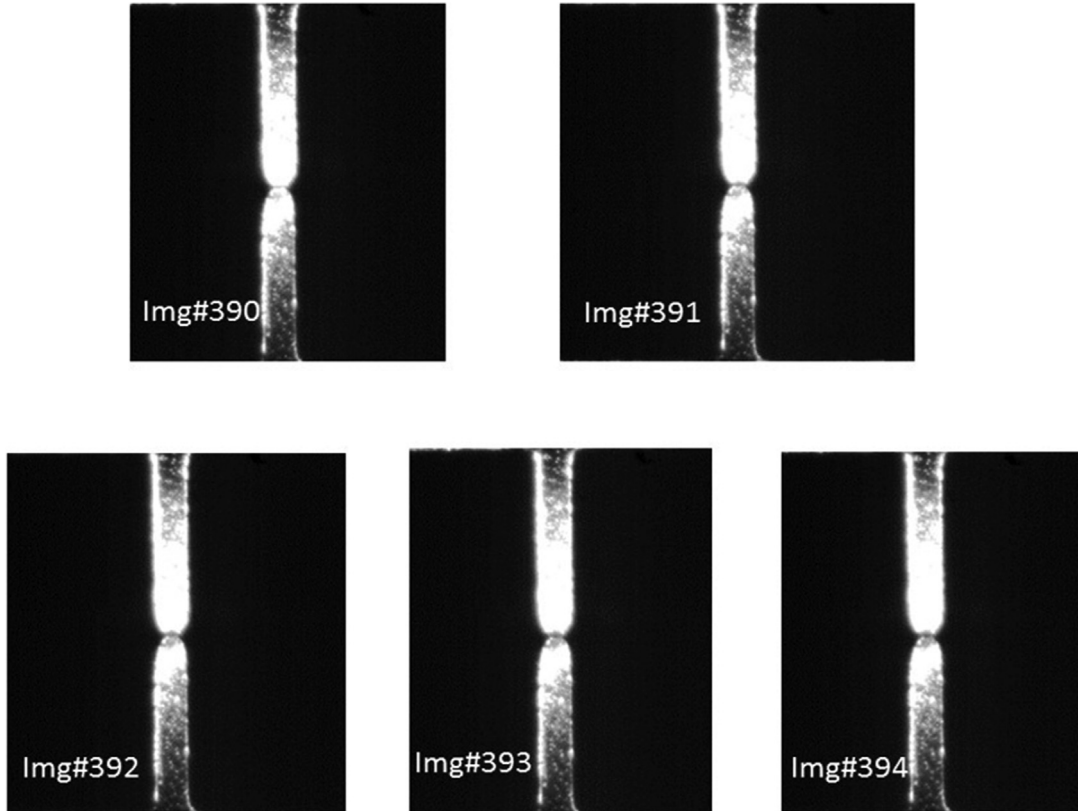


**Fig. 6** Sequence of images of a C-S1 specimen during the  $1 \text{ s}^{-1}$  test, during the time of fracture. This series of images illustrates the ambiguity in identifying the image where fracture occurs, for synchronization with the force's transition to force = 0. This range of images corresponds to an uncertainty in time of failure of 3.3 ms as the time between images is 0.67 ms.

fractures abruptly so there is no ambiguity in identifying the correct image for synchronization. Furthermore, the  $0.001 \text{ s}^{-1}$  test setup acquires both forces and images on the same computer so all  $0.001 \text{ s}^{-1}$  tests for both materials were automatically synchronized. In general, for test setups where forces and images are acquired by different systems, such as some in situ tests, the synchronization between the force data and images can be a source of uncertainty in the modulus.

*4.1.5 Summary of Young's Modulus Uncertainty Values Across All Material/Size/Rate Categories.* Table 9 summarizes the measurement uncertainty and relative standard deviations in the apparent Young's modulus for each material, when averaged over all specimen designs, at each strain rate. Since the measurement uncertainty exceeds the standard deviation in most of the material/size/rate categories (Table 2), the standard deviation cannot be associated with material variation. This may not be unusual for electrodeposited Nickel. One of the few papers that includes error analysis of LIGA tensile properties is an earlier study on Ni and NiFe by Mazza et al. [22] where at a strain of 0.002 their error in the Young's modulus (8%) exceeded their standard deviation (2%). As most studies to date do not include error analysis, the true variability in modulus for these materials is difficult to determine.

It should also be noted that the uncertainty in the apparent Young's modulus would be lower if analyzed at higher strains due to the larger displacements. However, the higher strains may also include greater microplasticity effects that are difficult to decouple from the apparent modulus, hence our choice of a relatively low nominal strain of  $5 \times 10^{-4}$  to 0.001 from which to extract the Young's modulus and its corresponding uncertainty. Microplasticity is discussed in Sec. 4.4.

**4.2 Challenges in Obtaining Young's Modulus From Tensile Tests.** It has been established in the conventional macro-scale mechanical testing community that the tensile test is not the

most reliable way to measure a material's Young's modulus, which is the property with the most variation even when the test is performed according to ASTM and international testing standards [26–28]. The reasons for this are exacerbated when the specimens are scaled down in size, thus it is not surprising that our measurement uncertainties are relatively high, the smallest uncertainty being 8% for the Alpha-S2 category (Table 2). These challenges include:

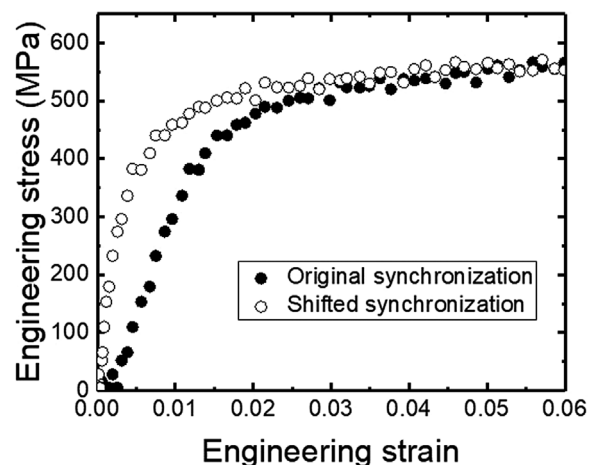


**Fig. 7** Part of the engineering stress–strain curve for the specimen from Fig. 6, when different images were used to synchronize the stresses and strains. The apparent Young's modulus is about 43 GPa for the original analysis, and about 129 GPa when the images were shifted by  $-7$  images (the negative sign indicates that the images in question occur after the one used for the original synchronization).

**Table 9 Summary of the measurement uncertainties and standard deviations in the apparent Young’s modulus at a nominal strain of 0.001, for each material and strain rate, with and without including the smallest (S4) specimens**

	Strain rate 0.001 s <sup>-1</sup>		Strain rate 1 s <sup>-1</sup>	
	Relative uncertainty %	CV %	Relative uncertainty %	CV %
Alpha	Without S4: <13 (with S4: 27)	9	Without S4: <50–80 (with S4: 126)	23
C	Without S4: <16–26 (with S4: 73)	22	<50–80	23

- (1) Specimen alignment and shifting in the grips at the start of the test. These can be difficult to eliminate completely, and yet can distort the stress–strain curve at the low strains corresponding to the linear elastic region. While this is frequently corrected for by slack compensation, for very small specimens there is limited displacement over which to get data in the early part of the linear elastic region that is free from slack. The specimens in this study were held by pins in clevises to allow for specimen self-alignment at the start of the test. Analyzing this source of uncertainty in specimen shifting and alignment is beyond the scope of this study.
- (2) Strain accuracy and resolution—the strain measurement technique must be able to measure the larger total strain at fracture as well as the much smaller strains in the linear elastic region. For DIC, the relative uncertainty in strain is not constant over the test but is higher for smaller strains.
- (3) Data analysis procedures—while fitting a straight line appears straightforward in principle, slight differences in fitting procedure or in the selection of data points can lead to significantly different slopes. A 2006 report by the National Physical Laboratory in the UK [26,27] summarized a European Union study where 15 EU participants analyzed the same set of raw data from conventional macroscale tensile tests. Even with the challenges in #1 and #2 being less severe than for micro and mesoscale specimens, up to 16% variation in the Young’s modulus was obtained from the same set of raw data, due to differences in data analysis procedures alone. A new ASTM standard—

ASTM E3076-18, published in 2019 [38]—addresses this by use of an algorithm that automatically determines the slope of a linear region of data using the least normalized residual, without operator input. This algorithm should reduce or eliminate the variation in Young’s modulus when the same set of stress–strain data is analyzed by different laboratories, provided the data meets the quality metrics defined in the standard.

- (4) For electrodeposited metals such as LIGA Ni and its alloys, microplasticity in the material is an additional factor.

**4.3 Challenges in Measuring Small Engineering Strains With Digital Image Correlation.** Figure 8(a) shows the displacements when a C specimen of the S3 design was loaded and unloaded at very low stresses and strains—a strain of  $5 \times 10^{-4}$  corresponded to a  $du$  of 1 pixel over a gauge length of 2000 pixels. When the same images were analyzed by two researchers independently, some unavoidable subjectivity arose in the analysts’ selection of regions for DIC, which led to a difference in  $du$  values of only 1 pixel. Yet, this difference, together with a second source of user-based subjectivity which is the selection of data points to include in the curve fit, can lead to over 50% difference in Young’s modulus values, as shown in (b). This illustrates #3 above, that differences in data analysis procedures alone can result in very different values of Young’s modulus even from the same raw data, in this case images.

As mentioned in #3 above, a new ASTM standard—ASTM 3076-18 [38]—uses an algorithm to determine the slope of a linear section of data without operator input. However, this approach

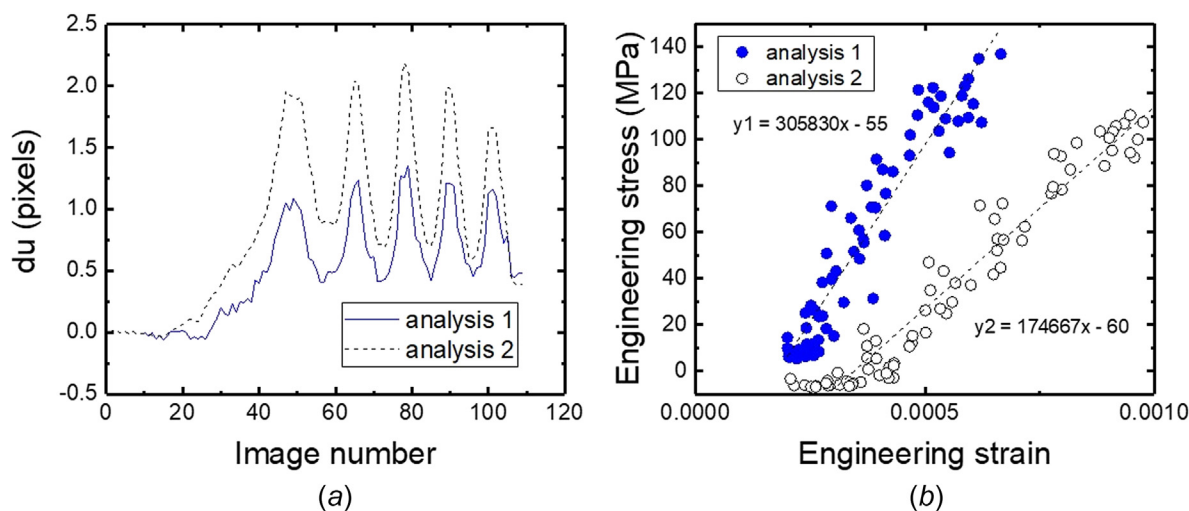


**Fig. 8 (a) Change in length (in pixels) of a C specimen of the S3 design (from an earlier fabrication run prior to the fabrication run in Tables 1 and 2), when cyclically loaded at strains below 0.001 to avoid microplasticity, and with the same images analyzed by two researchers independently. Subjectivity in selecting regions for DIC results in a difference of 1 pixel across a gauge length of 2000 pixels, between the two analyses. (b) Linear region of the stress–strain curve of the last loading cycle, resulting from the two DIC analyses in (a), and the resulting two values of apparent Young’s modulus (the slopes of the linear fits).**

begins with a given set of stress–strain data, i.e., an engineering stress–strain curve, and removes subjectivity in the fit to the linear portion of the curve. The uncertainty in the DIC (as in this discussion), however, leads to uncertainty in the raw displacements for computing the strains, i.e., it leads to uncertainty in the stress–strain curve itself. The small strains needed to avoid microplasticity (under  $\sim 0.001$  strain) in particular, result in large variations in DIC output as shown in Fig. 8, which in turn result in apparent Young’s modulus values that can vary significantly when the images are analyzed multiple times. Laser-based strain measurement techniques may provide smaller uncertainties at these small strains; an error analysis for those techniques would be needed to quantify their uncertainty.

These challenges with strain measurement and curve fitting, alone, should warn readers to exercise caution when using published values of Young’s modulus extracted from micro- and mesoscale tensile tests.

One way to experimentally resolve smaller engineering strains without modifying the imaging apparatus or software, is to fix one end of the specimen and take images only of the moving end. DIC can then be used to measure the absolute displacement (in units of length) of the free end. The disadvantage of this approach is that the engineering strain measurement is indirect since the gauge length has to be measured separately by other means, and the fixed end has to be assumed to be truly fixed because the resulting data cannot be corrected for specimen shifting. Furthermore, by capturing images not of the full gauge section but only of the free end, full-field strains, local strains, and other information of interest to plasticity and fracture analysis would be unavailable from the rest of the tensile test unless a second camera is added. This approach could, however, in principle be used to measure the apparent Young’s modulus outside of a tensile test, and which is used on conventionally sized specimens to mitigate uncertainties caused by specimen alignment and gripping, is to unload the specimen shortly after initial yielding and measure the unloading modulus, though this is outside the scope of this work and should be investigated in future work.

#### 4.4 Microplasticity in Lithographie, Galvanformung, Abformung Materials and Its Effect on the Young’s Modulus Uncertainty

4.4.1 *Microplasticity in Lithographie, Galvanformung, Abformung Materials.* Most metallic films, including Ni, not only exhibit variable properties due to extreme sensitivity to processing conditions (see the list of comparisons of previous literature for LIGA Ni summarized in Refs. [30] and [31]), they also experience

a transient in yield behavior during the first few cycles of fatigue loading, as well as significant room temperature creep. Other researchers have reported this to be a form of microplasticity [39], and thus we also refer to this phenomenon as such. Although our observations might also be related to elastic shakedown, more research would be needed to determine the mechanisms for our observations.

Microplasticity has been observed in LIGA materials, for example, El-Madhoun et al. [40] reported tests on annealed Ni where plastic strains several times larger than the elastic strain were produced between 100 and 200 MPa. Collins et al. [31] reported the apparent Young’s modulus to increase from 100 GPa to 160 GPa after prestraining at room temperature. Hemker and Last [41] found plastic strains in LIGA Ni at stresses below 200 MPa. They concluded that significant amounts of strain hardening occur in the early stages of the tensile test, below the proportional limit.

Microplasticity is therefore another factor that impedes extraction of the apparent Young’s modulus from tensile test data, because it may preclude the division of the total strain into an elastic and a plastic part. We first observed what we think is microplasticity by the fact that many specimens (at the quasi-static strain rate where the resolution of the images is higher) produced tensile curves with two distinct linear elastic regions [32,33], see Fig. 9. Although at first glance some may interpret the change in the slope to be indicative of the proportional limit, we believe Fig. 9 shows two distinct linear regions, because both regions have high linearity. More of such tensile curves can be found in the Appendix of Ref. [33]. The slope of the curve for strains up to  $5 \times 10^{-4}$  was typically higher than the slope at strains from  $5 \times 10^{-4}$  to  $\sim 0.01$  mm/mm. Since the specimens were preloaded, it is unlikely that the change in slope was an artifact from specimen shifting or machine compliance. The modulus values in Table 1 for the Alpha material at  $0.001 \text{ s}^{-1}$  were extracted from the high strain region. Given that the Young’s modulus is defined as the initial portion of the stress–strain curve, it would be more accurate to refer to  $E_1$  from Fig. 9 as the elastic modulus. Tests done at  $1 \text{ s}^{-1}$  showed only one linear region, perhaps due to the lower image resolution of the  $1 \text{ s}^{-1}$  test apparatus. (Not all specimens exhibited this phenomenon. Many specimens at the quasi-static rate also showed only one linear region, and many C specimens, in particular, also exhibited shorter and less distinct linear regions to begin with.)

4.4.2 *Cyclic Loading to Stabilize the Young’s Modulus.* We found further evidence of what we think is microplasticity by loading and unloading an Alpha specimen within its linear region

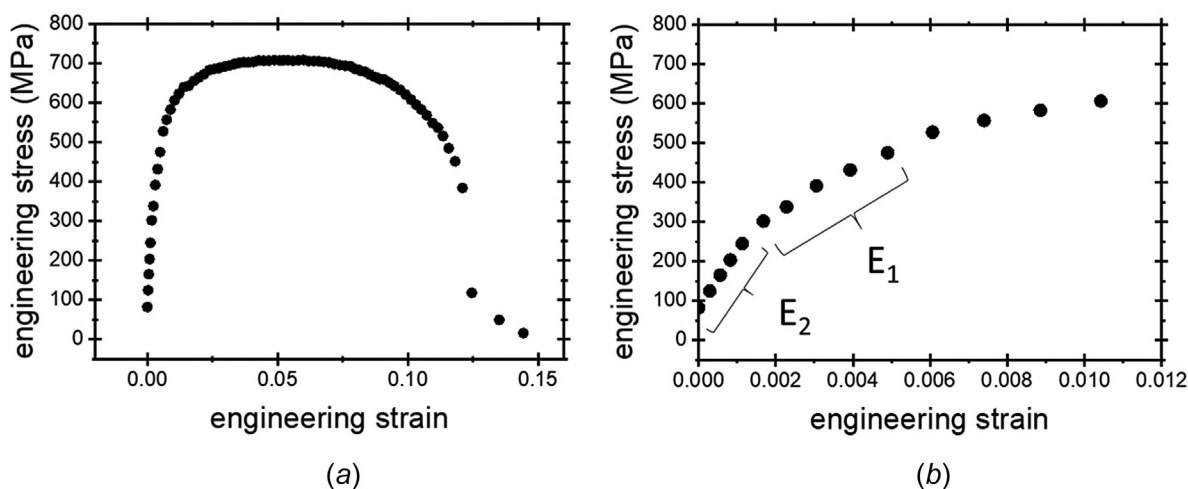


Fig. 9 (a) Engineering stress–strain curve of a C alloy specimen of the S2 design, tested at a strain rate of  $0.001 \text{ s}^{-1}$ . (b) Close up of the beginning of the curve in (a), showing two distinct linear elastic regions with associated apparent Young’s moduli “ $E_1$ ” and “ $E_2$ ”.

at up to 50% of the UTS, at a strain rate of  $0.001\text{ s}^{-1}$ , and measuring the apparent Young's modulus for each cycle, see Fig. 10(a). To reduce the measurement uncertainty, we selected the largest size specimen (S3), and the loading/unloading was performed in the higher strain range of 0.001–0.007 mm/mm. Figure 10(a) shows that the apparent Young's modulus increased by  $\sim 17\%$  from the first to the second loading cycle, and thereafter stayed constant within the measurement uncertainty for the next 14 cycles. At a nominal strain of 0.004, the measurement uncertainty was calculated at 3%.

In fact, as seen in Fig. 10(a), the most significant change in the modulus occurred during unloading of the first cycle. The small confidence intervals calculated on the slope of the stress–strain curves for the first cycle, shown in Fig. 10(b), suggest that this abrupt change in modulus is not an artifact. We believe this material behavior to be similar to the phenomenon reported by Collins et al. [31], where they did cyclic tests on LIGA Ni tensile specimens and also found the apparent Young's modulus to increase upon the first unloading. They also observed an increase in the yield strength and UTS, as well as decreases in the variability between specimens, after the cyclic loading. Collins et al. therefore recommended use of cyclic loading to stabilize the microstructure of LIGA MEMS devices before deployment, similar to the “burn in” of electronic devices. Even though our material chemistry, grain size, microstructure, and cyclic loading protocol differ somewhat from those of Collins et al., it appears that our alloys also stabilize in apparent Young's modulus after several load cycles (although further changes in the modulus may occur with more cycles).

While “microplasticity” is a general term that covers a variety of materials responses, we can make some reasonable inferences about the source of this behavior. As this transition between the two linear regions is fairly consistent [33], this suggests a transition between deformation regimes. Deformation below the yield strength generally comes under the heading of creep, which has different mechanisms depending upon stress and temperature. Recent research suggests that the regimes would also depend upon grain size [42]. Cao presents deformation maps where regimes are plotted as a function of stress and grain size (both normalized) based upon modeling [43]. The knee between the two linear regions observed in our materials occurs right around the transition from Coble (diffusional) creep to nanograin deformation. It is likely that the change in slope is due to a change in available deformation mechanisms. Cycling in the diffusional

creep regime might result in alterations in the grain configuration due to diffusional processes which can then reach a more stable configuration in which the nanograin deformation processes cannot easily dominate the mechanical response.

Note that the 3% measurement uncertainty here (the error bars in Fig. 10(a)) is not to be confused with the measurement uncertainties in the modulus that we reported in Sec. 4.1.5 and in Table 1, which are larger. The uncertainty for the *tensile* tests were higher because they were calculated at lower values of strain. For the Alpha specimens they were calculated at a nominal strain of 0.001, which for most specimens was the start of the high strain linear region. Smaller strains are associated with larger uncertainty, as discussed in Sec. 4.1.5, but are also less likely to include microplasticity effects. For the *cyclic loading* test, however, we calculated the uncertainty at a higher nominal strain of 0.004 which reduces the uncertainty in the strain. We also used the largest size specimen (S3) which also has the smallest uncertainty in strain due to its larger displacements. The objective of the cyclic loading test was to investigate whether quasi-static loading changes the value of apparent Young's modulus, in agreement with Collins et al.

A more general problem raised by microplasticity is how does one define the correct value of the Young's modulus for an application? Even if one could reliably measure the apparent Young's modulus at these low strains with small uncertainties—whether in a tensile test or using other methods—microplasticity reduces its applicability to device design and simulation if a MEMS device is loaded beyond this extent in a real-world application. Conversely, if one were to take the slope of the stress–strain curve at the higher strains, as we have done in Table 2 and Refs. [32] and [33], that value would be inappropriate for applications that never reach those strains as those materials in service would not have stabilized properties. Furthermore, even if a MEMS device is loaded to a higher strain in an application, there could still be changes in the apparent Young's modulus depending on the number of times the device is loaded. Our cyclic loading test on one specimen (Fig. 10(a)) suggested that the apparent modulus of the nanograined Ni-Fe material stabilized after one cycle, but Collins et al., who used a different cyclic loading protocol on pure Ni, found that stabilization of mechanical properties took many more cycles.

Therefore, it is our opinion that the proposal by Collins et al. to cyclically load LIGA MEMS devices before deployment to stabilize the material's microstructure and properties is a practical

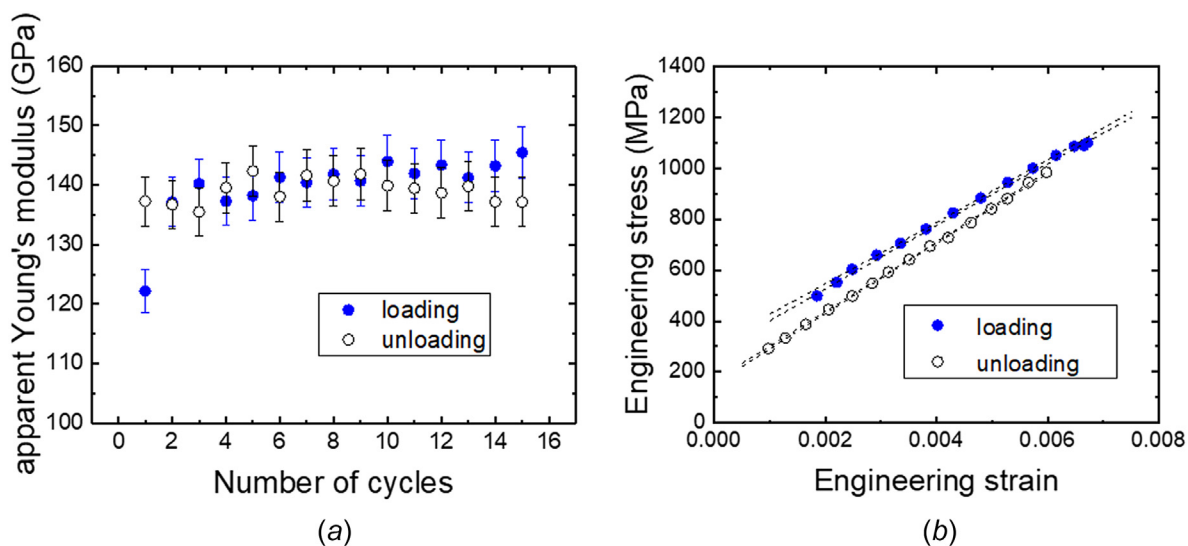


Fig. 10 (a) Apparent Young's modulus for each loading and unloading cycle within the linear elastic region of one Alpha S3 specimen. The error bars are the measurement uncertainty, calculated to be 3% at a nominal strain of 0.004. (b) Measured engineering stress and strain for the first loading and unloading cycle of the specimen from (a), and the calculated 95% confidence intervals on the slopes.

**Table 10** 0.002 offset yield strength, and its associated conventional relative uncertainty, total relative uncertainty, and relative standard deviation

Strain rate	Material	Design	Average yield strength (MPa)	Conventional uncertainty (%)	Total uncertainty (%)	CV (%)
0.001 s <sup>-1</sup>	Alpha	S1	1394	2	12	5
		S2	1432	1	8	5
		S3	1412	1	9	2
		S4	1282	10	29	4
	C	S1	411	3	26	4
		S2	447	3	18	9
		S3	437	2	17	11
		S4	402	8	41	10
1 s <sup>-1</sup>	Alpha	S1	1609	2	24	5
		S2	1619	1	35	6
		S3	1630	1	24	1
		S4	1502	6	34	5
	C	S1	435	4	44	27
		S2	505	2	40	17
		S3	525	2	54	3
		S4	438	13	51	4

solution to the microplasticity issue. In support of this, we suggest that the apparent Young’s modulus should also be measured from specimens which have had their microstructure stabilized by cyclic loading, in order to obtain elastic properties that can be more appropriately applied to device modeling and simulations. Alternatively, if the MEMS devices are not cyclically stabilized before deployment, a practical solution could be to determine the strain range over which the device is intended to function, and then determine the apparent Young’s modulus, from the tensile curves, over that same strain range.

## 5 Measurement Uncertainties in the 0.2% Offset Yield Strength

**5.1 Computation of the Measurement Uncertainty in the Yield Strength.** In Table 2 and Ref. [32], we reported the 0.2% offset yield strength and its associated uncertainties and standard deviations, for each alloy at each gauge size and strain rate. As shown in Table 2, the uncertainty in the yield strength ranged from 8% (Alpha, S3, 0.001 s<sup>-1</sup>) to over 50% (all 1 s<sup>-1</sup> tests). The uncertainties exceeded the standard deviations for *all* material/size/rate categories, in some cases significantly. Therefore, we were unable to quantify the material variability in the yield strength.

The uncertainty calculation was based on a procedure for conventional macroscale tensile tests, which resulted in what we refer to as the “conventional uncertainty” in the yield strength. This came out to be under 10% for all our specimen categories and in some categories was even under 5%. If we concluded the error analysis at this point, we could have claimed yield strength uncertainties of under 10%. However, we combined this uncertainty with the corresponding uncertainty in Young’s modulus, to obtain a “total uncertainty” in the yield strength, which we believe to be more realistic.

We first calculated the standard uncertainty based on the procedure by Matusevich et al. [44] and including techniques described by Morrison [45]. Our procedure is described in detail in Appendix A. Since the stress–strain curve differs slightly for each specimen, the standard uncertainty in the 0.2% offset yield stress (Eq. (A18) in Appendix A) was computed for each individual specimen. This value was then divided by that specimen’s yield stress to obtain what we call the “conventional relative uncertainty.” We refer to this as the “conventional” uncertainty because the analysis procedure followed that developed for conventional macroscale tensile tests.

As stated by Matusevich et al., however, this model does not account for other factors that can affect the repeatability and reproducibility of a tensile test but which are difficult to quantify

such as alignment of the specimen, testing rate, load frame or test procedure characteristics, etc. As discussed in Sec. 4.1.5, for the present mesoscale specimens the relative uncertainty in the apparent Young’s modulus can be over 50% depending on the material/size/rate combination. Since the Young’s modulus determines the slope of the 0.002 offset line and the shape of the stress–strain curve, the large uncertainty in Young’s modulus should not be ignored. In the preceding calculation of the conventional uncertainty, the slope of the stress–strain curve (and of the 0.002 offset line) is assumed to be a fixed parameter. To include the effect of the modulus uncertainty, we added the relative uncertainty in the modulus (from Sec. 4) in quadrature with the relative conventional uncertainty in the yield strength to obtain a final value which we call the *total relative uncertainty* in the yield strength. These are the uncertainty values reported in Table 2.

For all 1 s<sup>-1</sup> specimens as well as the C-S4 specimens, this resulted in a *total uncertainty* that was so large that the UTS could in principle be exceeded at the upper bound of the yield strength. Since this is not physically valid for ductile materials (the yield strength cannot exceed the UTS), for those specimen categories the value of the final error bar was adjusted to be that which would reach the UTS. Table 10 compares the *conventional uncertainty*, the *total uncertainty*, and the relative standard deviation, for each specimen category.

**5.2 Factors Influencing the Uncertainty in the Yield Strength.** The *conventional uncertainty* (Appendix A, Eq. (A18)) can be thought of as a measure of how well we “know” where the 0.002 offset line intersects the stress–strain curve. This is affected by the shape of the curve and how well the slope of the 0.002 offset line is known, as determined solely by how closely the data in the elastic region fits a straight line. The calculation assumes that any uncertainty in the 0.002 offset line’s slope is due only to possible deviations from linear behavior in the data. Our study of the modulus uncertainty (Sec. 4) was not concerned with the linearity of the data, however, but rather with how accurate the strain values are; the stress–strain curve may exhibit high linearity and yet the Young’s modulus values can be incorrect if the strain values are incorrect due to systematic strain measurement errors. This motivated the quadrature addition of the modulus uncertainty to the conventional uncertainty in the yield strength in an attempt to account for this effect. The result is the *total uncertainty* in Table 10. In most specimen categories, the modulus uncertainty dominates the yield strength’s total uncertainty as it is much larger than the conventional uncertainty.

However, the *total uncertainties* in Table 10 are still an estimate. The values are not exact because the nonlinear shape of the overall stress–strain curves results in the modulus uncertainty

affecting the yield strength uncertainty asymmetrically. For example, if the Young's modulus (and thus the slope of the 0.002 offset line) were to drop by 50%, the yield strength for most of our specimens will increase by less than 50% given that the stress-strain curve's slope decreases significantly with increasing strain in the plastic region, the curve being relatively flat (see Fig. 1). On the other hand, a 50% increase in Young's modulus could lead to a drastic reduction in yield strength given that the offset line would intersect the curve at a point much closer to the linear region where the stresses fall off more steeply with decreasing strain.

A more rigorous way to account for the nonsymmetric nature of this contribution, might be to reconstruct each specimen's stress-strain curve twice with different slopes in the linear region, corresponding to the upper and lower bounds of the Young's modulus. The difference between the new and nominal values of yield strength for each case would then constitute the contribution of the modulus uncertainty to the yield strength uncertainty and could then be added in quadrature with the conventional uncertainty in the yield strength. This calculation would be done separately for the lower and upper bound of the Young's modulus, thus resulting in two nonsymmetric values in the yield strength's uncertainty, per specimen. Reconstructing the stress-strain curves, however, could be nontrivial, given that the larger strains have lower uncertainty than the smaller strains and thus should not be adjusted. This could potentially lead to "gaps" in the curve between the reconstructed linear region and the plastic region where the new 0.002 offset line is likely to intersect, and thus result in another source of uncertainty.

Nevertheless, the *conventional uncertainty* alone (Eq. (A18)) does not account for the contribution of large uncertainties in Young's modulus arising from difficulties in strain measurement, and thus underestimates the error in the yield strength. For this study, the *total uncertainty* in yield strength exceeds the standard deviation for all material/size/rate categories (Table 10), because the modulus uncertainty is relatively large. Therefore, the standard deviation should not be attributed to material variability. Also, the *total uncertainties* were much higher at  $1 \text{ s}^{-1}$  than at  $0.001 \text{ s}^{-1}$  and were also higher for the C alloy than the Alpha. The lowest uncertainties were for the larger size (S2 and S3) Alpha specimens at  $0.001 \text{ s}^{-1}$ , which is expected since the larger specimens had larger displacements and thus lower uncertainties in strain.

Material microplasticity, discussed in Sec. 4, also contributes to the uncertainty in the yield strength, as many Alpha specimens and some C specimens exhibited two distinct linear regions in their stress-strain curves (the stress-strain curves can be found in the Appendix of Ref. [33]). For these specimens, the choice of which linear region to use for the Young's modulus and the 0.002 offset line, would lead to very different values of yield strength. For the purposes of this study, whenever a specimen exhibited two distinct linear regions we chose the high strain region to determine its apparent Young's modulus and 0.002 offset yield strength, as discussed in Ref. [33]. Because of these microplasticity effects, prestraining the specimen might reduce the uncertainty in the yield strength. Finally, note that the 0.002 offset strain value is just a convention, and in practice the yield strength is sometimes defined at higher specific values of strain.

As with the Young's modulus, it is our opinion that consideration of these factors affecting the uncertainty in the yield strength could be relevant to other studies on LIGA tensile properties. Literature values of 0.002 offset yield strength for LIGA materials should be used with caution, especially if the associated measurement uncertainties are not given.

## 6 Measurement Uncertainties in the Strain Hardening Exponent and Strength Coefficient

**6.1 Computation of the Measurement Uncertainties in  $n$  and  $A$ .** In Table 3 and Ref. [32], we reported the strain hardening exponent,  $n$ , and strength coefficient,  $A$ , for both alloys at both strain rates. Given the overall absence of size- and rate effects on

**Table 11 Strain hardening exponent,  $n$ , and strength coefficient,  $A$ , for both materials, averaged over all specimens, and the relative standard deviations. The measurement uncertainties were smaller than the standard deviations, and size- and rate effects were found to be nonexistent or small.**

All sizes and rates	$n$ , average	CV (%)	$A$ (MPa), average	CV (%)
Alpha	0.11	25	3048	10
C	0.13	17	1069	15

the strain hardening parameters, Table 11 shows the final values of  $n$  and  $A$  when averaged over all specimens. For all material/size/rate combinations, the errors were found to be comparable to or smaller than the standard deviations, thus the overall uncertainty in the strain hardening is dominated by the material variability. We now discuss how the errors were calculated:

As described in Ref. [32],  $n$  and  $A$  were extracted for each specimen by fitting the tensile data, in the region between the 0.002 offset yield and the UTS (which occurs before the onset of necking), to the Hollomon equation [46]

$$\sigma_t = A \varepsilon_p^n \quad (1)$$

where  $\sigma_t$  is the true stress and  $\varepsilon_p$  is the true plastic strain. Equation (1) is also used in the ASTM-E646 standard for determining the strain hardening exponents of sheet metals [47]. When  $\text{Log}(\sigma_t)$  versus  $\text{Log}(\varepsilon_p)$  is plotted the data approximates a straight line with slope  $n$  and  $\text{Log}(A)$  as the intercept with the vertical axis. Since  $n$  is the slope of a straight line, the uncertainty in  $n$  is therefore the uncertainty in the slope of a linear least squares fit, which can be calculated by established statistical methods. This was done for each individual specimen, due to slight differences in each specimen's stress-strain curve which resulted in different degrees of fit to the Hollomon equation. Details of our calculation procedure are in Appendix B.

For both materials, the uncertainty in  $n$  is less than 10% and the uncertainty in  $A$  is less than 5%, for all but the smallest (S4) specimens. For the S4 specimens, however, the uncertainty in  $n$  was 8–30% for the  $0.001 \text{ s}^{-1}$  tests and 7–28% for the  $1 \text{ s}^{-1}$  tests, while the error in  $A$  was 2–12% for  $0.001 \text{ s}^{-1}$  and 4–9% for  $1 \text{ s}^{-1}$ , as tabulated in Table 3. As with the measurement uncertainty in the apparent Young's modulus, the uncertainties were larger for the S4 specimens because the uncertainty in strain is higher for the smallest specimens due to their smaller displacements and fewer pixels in the images of the shorter gauge lengths. The uncertainty in force is also slightly higher for the S4 specimens at  $1 \text{ s}^{-1}$  due to the small forces being at the extreme low end of that load cell's range. (Whereas the loadcell for the  $1 \text{ s}^{-1}$  tests had an uncertainty of 1% of the reading according to the manufacturer, we calibrated the uncertainty to be about 3% for the range of 1–20 N, which is the force range seen by the S4 specimens.)

**6.2 Additional Factors Influencing the Uncertainty in  $n$  and  $A$ .** One might argue that we should add the above uncertainties in  $n$  and  $A$  in quadrature with the uncertainties in Young's modulus and UTS since the modulus and UTS determine the range on the tensile curve for fitting the power law equation. We did not do this, however. The uncertainty in UTS is so low (2%) that it would have negligible impact. On the other hand, the uncertainty in Young's modulus is so high (10% for some material/size/rate categories and over 50% for other categories) that it would lead to such artificially high values of uncertainty for  $n$  and  $A$  such that the latter would no longer be physically meaningful or practical. (For example, adding an 80% uncertainty in Young's modulus to the uncertainty in  $n$  would increase the uncertainty in  $n$  to  $\sim 80\%$ , which does not make physical sense because the slope of the Log-Log plot of Eq. (1) does not vary by 80% from simply changing the Young's modulus by this amount, due to the shape of

the stress–strain curve. Similarly, an ~80% uncertainty in  $A$  is not physically meaningful because the strength coefficient is comparable to the UTS which does not have an 80% uncertainty.) As with the yield strength uncertainty, a possible way to capture the effect of the Young’s modulus uncertainty on the strain hardening might be to reconstruct the stress–strain curve twice, using the upper and lower bounds of the modulus, and from there perform the above computations of the strain hardening uncertainty to obtain new upper and lower bounds on the uncertainties in  $n$  and  $A$ .

Another source of uncertainty is the choice of power-law model. As stated in Ref. [48], there is nothing fundamental about the Hollomon equation (Eq. (1)), and variations such as the Ludwik equation [49] are also widely used, with different equations providing better fits for different materials. We found that the Ludwik equation resulted in up to  $4\times$  increase in  $n$  for the present materials [32]. The  $n$  and  $A$  reported by Namazu and Inoue [50] was much higher than that reported by Williams [51], Lou et al. [52], and in this study. The specimens in these studies all differ in chemistry, microstructure and size, but are all electrodeposited Ni or Ni alloys. Like Williams and Lou et al., we used the Hollomon model and our strain hardening values are similar to theirs, while the values of Namazu and Inoue are much higher, their use of the Ludwik equation could be a factor. Microplasticity is another potential source of error as it affects the 0.002 offset yield strength or the lower bound of the range of data for extracting the strain hardening parameters. Ductility is yet another source of uncertainty. All of these factors are difficult to quantify, however.

**6.3 Statistical Variations in the Strain Hardening Parameters.** The statistical variations in  $n$  and  $A$ , represented by the standard deviations, are comparable to or larger than the measurement uncertainty for all material/rate/size categories, see Table 3. Therefore, the standard deviation represents the variability in the specimen material itself and dominates the overall uncertainty in the strain hardening parameters for both materials. For both alloys the standard deviation in  $n$  is also larger at  $1\text{ s}^{-1}$  than at  $0.001\text{ s}^{-1}$ , but, due to the small sample populations (three specimens in each material/rate/geometry category), this trend is probably insignificant.

Strain rate appears not to affect the standard deviation in  $A$  for the Alpha material. But for the C material the standard deviation is *lower* for the  $1\text{ s}^{-1}$  tests than for the  $0.001\text{ s}^{-1}$  tests, but again the small population size in each category could make this trend insignificant. Overall, the C specimens show a higher standard deviation in  $A$  than the Alpha specimens, across both strain rates. This could be explained as follows. The C specimens’ stress–strain curves are relatively flat at the top, thus the maximum stress could differ very slightly from the neighboring stress values due to noise but would still be identified as the UTS. This leads to greater statistical variation in the strain-to-UTS, and thereby in the range of data for fitting the power law equation (Eq. (1)). The Alpha material, on the other hand, being more brittle, does not elongate as much and thus there is less variation in the range of data for extracting the strain hardening parameters. The result is the standard deviation in  $A$  is expected to be greater for the more ductile C material, as found.

## 7 Summary

In Ref. [32], we reported the apparent Young’s modulus, yield strength, UTS, and strain hardening exponent and strength coefficient for two LIGA Ni alloys of thickness  $200\text{ }\mu\text{m}$ , tested at strain rates  $0.001\text{ s}^{-1}$  and  $1\text{ s}^{-1}$ , and for four gauge widths ranging from  $75\text{ }\mu\text{m}$  to  $700\text{ }\mu\text{m}$ . In this paper, we discussed the associated measurement uncertainties. Our measurement uncertainties were comparable to or smaller than the standard deviation for the UTS and strain hardening parameters. For the Young’s modulus the measurement error was under 10% for only two specimen categories, while for all other material/rate/size combinations the uncertainty was much greater and exceeded the standard deviation. For the 0.002 offset yield strength, the uncertainty exceeded the standard deviation for all specimens once we included the

influence of the modulus uncertainty. We also discussed challenges with obtaining the Young’s modulus from mesoscale tensile tests and propose that for electrodeposited films, such as LIGA alloys, the Young’s modulus be measured from specimens that have undergone cyclic loading in the elastic region to stabilize their microstructure. Despite the many studies on LIGA mechanical properties published to date, relatively few papers report the associated measurement uncertainties. Due to the well-documented variability in properties of electrodeposited metals, an understanding of the measurement uncertainties in micro- and mesoscale tensile tests can therefore help the reader to interpret the variations in literature values and appropriately apply the reported properties. Particular caution should be exercised when using values of Young’s modulus and 0.2% yield strength.

## Acknowledgment

We thank Dash Weeks, Frank DelRio, Nicholas Barbosa, and Todd Christenson for helpful discussions. Specific commercial equipment, instruments, and materials that are identified in this report are listed in order to adequately describe the experimental procedure and are not intended to imply endorsement or recommendation by the National Institute of Standards and Technology (NIST). The JFTP project number was 14-G-006, Micro-Scale Materials and Energetic Effects Characterization.

## Funding Data

- U.S. Army Combat Capabilities Development Command Armaments Center (CCDC AC) (Funder ID: 10.13039/100006751).
- Joint Fuze Technology Program (JFTP) (Funder ID: 10.13039/100000005).

## Data Availability Statement

The datasets generated and supporting the findings of this article are obtainable from the corresponding author upon reasonable request.

## Appendix A: Calculation of the Conventional Uncertainty in Yield Strength

The conventional uncertainty was calculated based on the procedure by Matusевич et al. [44] and using techniques from Ref. [45]. This uncertainty was calculated for each individual specimen, since the stress–strain curve differs slightly for each specimen. First, we find the equation of the straight line that comprises the linear elastic region of the force–displacement curve (line 1), where the displacement is the specimen displacement (not the machine displacement) using linear least squares regression. We then find the equation of line 2 which is parallel to line 1 but offset by 0.2% of the initial gauge length. The two lines are given by.

$$y_1 = mx + b_1 \quad (\text{A1})$$

$$y_2 = mx + b_2 \quad (\text{A2})$$

where  $y_1$  and  $y_2$  are the measured forces,  $x$  is the measured displacement,  $m$  is the slope of both lines, and  $b_1$  and  $b_2$  are their respective  $y$ -intercepts. Next, the intersection of the force–displacement curve with line 2 is found. In the immediate vicinity of the intersection the curve can be approximated as a straight line, line 3

$$y_3 = m_3x + b_3 \quad (\text{A3})$$

The *yield force* is found by equating lines 2 and 3 (Eqs. (A2) and (A3))

$$F_y = \frac{mb_3 - m_3b_1 + \beta mm_3L_e}{m - m_3} \quad (\text{A4})$$

where  $L_e$  is the original gauge length and  $\beta$  is 0.2%. Since  $F_y$  and  $A_o$  (the original cross-sectional area) are uncorrelated, their sensitivity coefficients are calculated

$$c_{F_y} = \frac{1}{A_0}, \quad c_{A_0} = \frac{-F_y}{A_0^2} \quad (\text{A5})$$

The sensitivity coefficients for  $m$ ,  $m_3$ ,  $b_1$ ,  $b_3$ , and  $L_e$ , are also calculated

$$c_{b_1} = \frac{-m_3}{m - m_3} \quad (\text{A6})$$

$$c_m = \frac{m_3(b_1 - b_3 - \beta L_e m_3)}{(m - m_3)^2} \quad (\text{A7})$$

$$c_{b_3} = \frac{m}{m - m_3} \quad (\text{A8})$$

$$c_{m_3} = \frac{m(b_3 - b_1 - \beta L_e m)}{(m - m_3)^2} \quad (\text{A9})$$

$$c_{L_e} = \beta \frac{m m_3}{m - m_3} \quad (\text{A10})$$

The covariance of  $m$ ,  $m_3$ ,  $b_1$ , and  $b_3$  are then calculated. Here we deviated from Matusевич et al. in that they used a weighted total least-squares approach whereas we used an ordinary least squares approach for simplicity, in a manner similar to that described by Morrison [45]. The standard deviation of an arbitrary straight line  $y(x)$  is given by

$$s_{y,x} = \sqrt{\frac{SS_E}{n-2}} \quad (\text{A11})$$

where  $n$  is the number of data points, and  $SS_E$  is the sum of squared error between the data and the fitted line, and is given by

$$SS_E \equiv \sum_{i=1}^n (y_i - \hat{y}_i)^2 \quad (\text{A12})$$

where the linear model to be fitted is  $\hat{y} = \hat{m}x + \hat{b}$ . We then find the standard deviation of the slope,  $u(m)$

$$u(m) = s_m = \sqrt{\frac{S_{y,x}^2}{SS_{xx}}} \quad (\text{A13})$$

where  $SS_{xx}$  is the sum squared error between the data and the mean

$$SS_{xx} \equiv \sum_{i=1}^n (x_i - \bar{x})^2 \quad (\text{A14})$$

If the line's  $y$ -intercept is  $b$ , the standard deviation of  $b$  is then given by

$$u(b) = s_b = \sqrt{s_{y,x}^2 \left( \frac{1}{n} + \frac{\bar{x}^2}{SS_{xx}} \right)} \quad (\text{A15})$$

where  $\bar{x}$  is the average of all the  $x$  values. Using Eqs. (A11)–(A15),  $u(m)$  and  $u(b)$  are calculated for lines 1 and 3. The covariance of the slopes and intercepts for lines 1 and 3 are then calculated [45]

$$u(m, b) = \text{Cov}(\hat{m}, \hat{b}) = -\frac{(s_{y,x}^2)(\bar{x})}{SS_{xx}} \quad (\text{A16})$$

Next, the sensitivity coefficients (Eqs. (A6)–(A10)) and the standard deviations in the slopes and intercepts and covariances for lines 1 and 3 (Eqs. (A13), (A15), and (A16)), applied to lines 1 and 3) are used to calculate the uncertainty in the yield force,  $u(F_y)$ , given in Ref. [44]

$$u(F_y) = \sqrt{[c_{b_1}u(b_1)]^2 + [c_m u(m)]^2 + [c_{b_3}u(b_3)]^2 + [c_{m_3}u(m_3)]^2 + [c_{L_e}u(L_e)]^2 + 2c_{b_1}c_m u(b_1, m) + 2c_{b_3}c_{m_3}u(b_3, m)} \quad (\text{A17})$$

Finally, the uncertainty in  $F_y$  (Eq. (A17)), and the sensitivity coefficients for  $F_y$  and  $A_o$  (Eq. (A5)) are used to calculate the standard uncertainty in the yield stress [44]

$$u(S_y) = \sqrt{[c_{F_y}u(F_y)]^2 + [c_{A_o}u(A_o)]^2} \quad (\text{A18})$$

The standard uncertainty in the 0.2% offset yield stress (Eq. (A18)) was computed for each individual specimen, and then divided by that specimen's yield stress to obtain what we call the conventional relative uncertainty. We refer to this as the conventional uncertainty because the analysis procedure followed that developed for conventional macroscale tensile tests.

## Appendix B: Calculation of the Uncertainties in the Strain Hardening Exponent and Strength Coefficient

As described in Ref. [32], the strain hardening exponent,  $n$ , and strength coefficient,  $A$ , were extracted for each specimen by fitting the tensile data, in the region between the 0.002 offset yield and the UTS (which occurs before the onset of necking), to the Hollomon equation [46]

$$\sigma_t = A \varepsilon_p^n \quad (\text{B1})$$

where,  $\sigma_t$  is the true stress, and  $\varepsilon_p$  is the true plastic strain. From Ref. [45], for a linear least squares fit the uncertainty in the slope can be found by first calculating the standard deviation of the slope, where “ $x$ ” is the independent variable (in this case,  $\text{Log}(\varepsilon_p)$ ) and “ $y$ ” is the dependent variable (in this case,  $\text{Log}(\sigma_t)$ )

$$s_m = \sqrt{\frac{S_{y,x}^2}{SS_{xx}}} \quad (\text{B2})$$

where  $S_{y,x}^2$  is the variance in  $y$  or variance in  $\text{Log}(\sigma_t)$ , and  $SS_{xx}$  is given by

$$SS_{xx} \equiv \sum_{i=1}^N (x_i - \bar{x})^2 \quad (\text{B3})$$

where  $N$  is the number of data points. The 95% confidence interval on the slope  $m$  of the linear regression is then calculated using the  $t$ -distribution with  $(N - 2)$  degrees-of-freedom

$$m + / - t_{0.025, N-2, s_m} \quad (\text{B4})$$

For these data, the value of  $t_{0.025, N-2}$  is typically around 2. Therefore, the size of the error bars for the strain hardening exponent in Ref. [32] are given by the “ $\pm$ ” part of Eq. (B4), and

are unique to each specimen because each specimen's tensile curve will have different linear fit parameters (the values are similar across the specimens within the same category, though).

To find the uncertainty in  $A$ , we first find the uncertainty in the  $y$ -intercept of the Log–Log plot. From Ref. [45], if  $b$  is the intercept of the Log–Log plot, then its uncertainty is given by

$$b \pm t_{0.025, N-2, s_b} \quad (\text{B5})$$

where  $b = \text{Log}(A)$ , and  $s_b$  is given by

$$s_b = \sqrt{s_{y,x}^2 \left( \frac{1}{N} + \frac{\bar{x}^2}{SS_{xx}} \right)} \quad (\text{B6})$$

Equations (B5) and (B6) give the uncertainty in the  $y$ -intercept of the Log–Log plot, or the uncertainty in  $\text{Log}(\sigma_t)$  at  $\varepsilon_p = 1$ , where the value of  $\sigma_t$  is  $A$ . Then, since

$$A = 10^b \quad (\text{B7})$$

Therefore

$$\frac{d}{db}(A) = (A)(\ln 10) \quad (\text{B8})$$

From Eq. (B8), the relative uncertainty in  $A$  is therefore

$$\frac{dA}{A} = (\ln 10) db \quad (\text{B9})$$

## References

- [1] Safranek, W. H., 1986, *The Properties of Electrodeposited Metals and Alloys: A Handbook*, American Electroplaters Society, Orlando, FL.
- [2] Dini, J. W., 1993, *Electrodeposition: The Materials Science of Coatings and Substrates*, Noyes Publications, Park Ridge, NJ.
- [3] Becker, E. W., Ehrfeld, W., Hagmann, P., Maner, A., and Munchmeyer, D., 1986, "Fabrication of Microstructures With High Aspect Ratios and Great Structural Heights by Synchrotron Radiation Lithography, Galvanoformung, and Plastic Moulding (LIGA Process)," *Microelectron. Eng.*, **4**(1), pp. 35–56.
- [4] Ehrfeld, W., Bley, P., Gotz, F., Hagmann, P., Maner, A., Mohr, J., Moser, H. O., Munchmeyer, D., Schelb, W., Schmidt, D., and Becker, E. W., 1987, "Fabrication of Microstructures Using the LIGA Process," Proceedings of the IEEE Micro Robots and Teleoperators Workshop, Piscataway, NJ, Nov. 9–11, pp. 1–11.
- [5] Guckel, H., Christenson, T. R., Skrobis, K. J., Denton, D. D., Choi, B., Lovell, E. G., Lee, J. W., Bajikar, S. S., and Chapman, T. W., 1990, "Deep X-ray and UV Lithographies for Micromechanics," *Proceedings of the IEEE 4th Technical Digest on Solid-State Sensor and Actuator Workshop*, Hilton Head Island, SC, June 4–7, pp. 118–122.
- [6] Christenson, T. R., and Guckel, H., 1995, "Deep X-ray Lithography for Micromechanics," *Proc. SPIE* **2639**, pp. 134–145.
- [7] Woo, Y., and Kim, S.-H., 2011, "Sensitivity Analysis of Plating Conditions on Mechanical Properties of Thin Film for MEMS Applications," *J. Mech. Sci. Technol.*, **25**(4), pp. 1017–1022.
- [8] Wang, N., Wang, Z., Aust, K. T., and Erb, U., 1997, "Room Temperature Creep Behavior of Nanocrystalline Nickel Produced by an Electrodeposition Technique," *Mater. Sci. Eng., A*, **237**(2), pp. 150–158.
- [9] Li, H., and Ebrahimi, F., 2006, "Tensile Behavior of a Nanocrystalline Ni-Fe Alloy," *Acta Mater.*, **54**(10), pp. 2877–2886.
- [10] Schwaiger, R., Reszat, J.-T., Bade, K., Aktaa, J., and Kraft, O., 2009, "A Combined Microtensile Testing and Nanoindentation Study of the Mechanical Behavior of Nanocrystalline LIGA Ni-Fe," *Int. J. Mater. Res. (Formerly Z. Metallkd.)*, **100**(1), pp. 68–75.
- [11] Haque, M. A., and Saif, M. T. A., 2003, "A Review of MEMS-Based Microscale and Nanoscale Tensile and Bending Testing," *Exp. Mech.*, **43**(3), pp. 248–255.
- [12] Sharpe, W. N., 2003, "Murray Lecture: Tensile Testing at the Micrometer Scale: Opportunities in Experimental Mechanics," *Exp. Mech.*, **43**(3), pp. 228–237.
- [13] Sharpe, W. N., Bagdahn, J., Jackson, K., and Coles, G., 2003, "Tensile Testing of MEMS Materials—Recent Progress," *J. Mater. Sci.*, **38**(20), pp. 4075–4079.
- [14] Sharpe, W. N., 2008, "Mechanical Property Measurement at the Micro/Nano-Scale," *Strain*, **44**(1), pp. 20–26.
- [15] Hemker, K. J., and Sharpe, W. N., 2007, "Microscale Characterization of Mechanical Properties," *Annu. Rev. Mater. Res.*, **37**(1), pp. 93–126.
- [16] Sharpe, W. N., Jr., 1982, "Applications of the Interferometric Strain/Displacement Gage," *Opt. Eng.*, **21**(3), pp. 483–488.
- [17] Sharpe, W. N., Jr., and Fowler, R. O., 1993, "A Novel Miniature Tension Test Machine," *Small Specimen Test Techniques Applied to Nuclear Reactor Vessel Thermal Annealing and Plant Life Extension*, W. R. Corwin, F. M. Haggag, and W. L. Server, eds., ASTM, Philadelphia, PA.
- [18] Sharpe, W. N., Jr., Yuan, B., and Edwards, R. L., 1997, "A New Technique for Measuring the Mechanical Properties of Thin Films," *J. Microelectromech. Syst.*, **6**(3), pp. 193–199.
- [19] Zupan, M., and Hemker, K. J., 2002, "Application of Fourier Analysis to the Laser Based Interferometric Strain/Displacement Gage," *Exp. Mech.*, **42**(2), pp. 214–220.
- [20] Sutton, M. A., Ortu, J. J., and Schreier, H., 2009, *Image Correlation for Shape, Motion and Deformation Measurements: Basic Concepts, Theory and Applications*, Springer, New York.
- [21] Pan, B., Qian, K., Xie, H., and Asundi, A., 2009, "Two-Dimensional Digital Image Correlation for in Plane Displacement and Strain Measurement: A Review," *Meas. Sci. Technol.*, **20**(6), p. 062001.
- [22] Mazza, E., Abel, S., and Dual, J., 1996, "Experimental Determination of Mechanical Properties of Ni and Ni-Fe Microbars," *Microsyst. Technol.*, **2**(4), pp. 197–202.
- [23] Chasiotis, I., and Knauss, W. G., 2002, "A New Microtensile Tester for the Study of MEMS Materials With the Aid of Atomic Force Microscope," *Exp. Mech.*, **42**(1), pp. 51–57.
- [24] Banks-Sills, L., Shklovsky, J., Krylov, S., Bruck, H. A., Fourman, V., Eliasi, R., and Ashkenazi, D., 2011, "A Methodology for Accurately Measuring Mechanical Properties on the Micro-Scale," *Strain*, **47**(3), pp. 288–300.
- [25] Stephens, L. S., Kelly, K. W., Simhadri, S., McCandless, A. B., and Meletis, E. I., 2001, "Mechanical Property Evaluation and Failure Analysis of Cantilevered LIGA Nickel Microposts," *J. Microelectromech. Syst.*, **10**(3), pp. 347–359.
- [26] Lord, J. D., and Morrell, R., 2006, "Measurement Good Practice Guide No. 98: Elastic Modulus Measurement," National Physical Laboratory, Teddington, UK, Report No. 98.
- [27] Lord, J. D., and Morrell, R. M., 2010, "Elastic Modulus Measurement—Obtaining Reliable Data From the Tensile Test," *Metrologia*, **47**(2), pp. S41–S49.
- [28] Davis, J. R. (Ed.), 2004, *Tensile Testing*, 2nd ed., ASM International, Materials Park, OH.
- [29] Yang, Y., Imasogie, B. I., Allameh, S. M., Boyce, B., Lian, K., Lou, J., and Soboyejo, W. O., 2007, "Mechanisms of Fatigue in LIGA Ni MEMS Thin Films," *Mater. Sci. Eng., A*, **444**(1–2), pp. 38–50.
- [30] Tang, J., Wang, H., Li, S. C., Liu, R., Mao, S. P., Li, X. P., Zhang, C. C., and Ding, G., 2009, "Design and Fabrication of a Micron Scale Free-Standing Specimen for Uniaxial Micro-Tensile Tests," *J. Micromech. Microeng.*, **19**(10), p. 105015.
- [31] Collins, J. G., Wright, M. C., and Muhlstein, C. L., 2011, "Cyclic Stabilization of Electrodeposited Nickel Structural Films," *J. Microelectromech. Syst.*, **20**(3), pp. 753–763.
- [32] Liew, L. A., Read, D. T., Martin, M. L., DeRiio, F. W., Bradley, P. E., Barbosa, N., Christenson, T., and Geaney, J., 2021, "Elastic-Plastic Properties of Mesoscale Electrodeposited LIGA Nickel Alloy Films: Microscopy and Mechanics," *J. Micromech. Microeng.*, **31**(1), p. 015002.
- [33] Liew, L. A., Read, D. T., White, R., and Barbosa, N., 2018, "US Army ARDEC Joint Fuze Technology Program (JFTP) Task 2 Report: Quasi-Static Tensile Tests of Microfabricated Electrodeposited (LIGA) Ni Alloys," National Institute of Standards and Technology, Gaithersburg, MD, NIST Interagency/Internal Report No. 8182.
- [34] Liew, L. A., Read, D. T., Martin, M. L., Christenson, T. R., and Geaney, J., 2021, "Microfabricated Fiducial Markers for Digital Image Correlation-Based Micromechanical Testing of LIGA Ni Alloys," *Eng. Res. Express*, **3**(2), p. 025019.
- [35] Taylor, J. R., 1997, *An Introduction to Error Analysis: The Study of Uncertainties in Physical Measurements*, 2nd ed., University Science Books, Sausalito, CA.
- [36] Fritz, T., Griepentrog, M., Mokwa, W., and Schnakenberg, U., 2003, "Determination of Young's Modulus of Electroplated Nickel," *Electrochim. Acta*, **48**(20–22), pp. 3029–3035.
- [37] Berfield, T. A., Patel, J. K., Shimmin, R. G., Braun, P. V., Lambros, J., and Sottos, N. R., 2007, "Micro- and Nanoscale Deformation Measurement of Surface and Internal Planes Via Digital Image Correlation," *Exp. Mech.*, **47**(1), pp. 51–62.
- [38] ASTM, 2019, "Standard Practice for Determination of the Slope in the Linear Region of a Test Record," ASTM International, West Conshohocken, PA, ASTM Standard No. ASTM E3076-18.
- [39] Maaß, R., and Derlet, P. M., 2018, "Micro-Plasticity and Recent Insights from Intermittent and Small-Scale Plasticity," *Acta Mater.*, **143**, pp. 338–363.
- [40] El-Madhoun, Y., Mohamed, A., and Bassim, M. N., 2004, "Cyclic Stress-Strain Behavior of Polycrystalline Nickel," *Mater. Sci. Eng., A*, **385**(1–2), pp. 140–147.
- [41] Hemker, K. J., and Last, H., 2001, "Microsample Tensile Testing of LIGA Nickel for MEMS Applications," *Mater. Sci. Eng., A*, **319–321**, pp. 882–886.
- [42] Kawasaki, M., and Langdon, T., 2013, "The Many Facets of Deformation Mechanism Mapping and the Application to Nanostructured Materials," *J. Mater. Res.*, **28**(13), pp. 1827–1834.

- [43] Cao, F., 2015, "Incorporating Dislocation Variables Into Mohamed's and Kawasaki-Langdon's Deformation Mechanism Maps Containing Superplasticity Mechanism Regimes," *Mater. Sci. Eng.: A*, **643**, pp. 169–174.
- [44] Matusевич, A. E., Massa, J. C., and Mancini, R. A., 2013, "Computation and Uncertainty Evaluation of Offset Yield Strength," *J. Test. Eval.*, **41**(2), pp. 217–230.
- [45] Morrison, F. A., 2014, "Obtaining Uncertainty Measures on Slope and Intercept of a Least Squares Fit With Excel's LINEST," *Department of Chemical Engineering*, Michigan Technological University, Houghton, MI.
- [46] Hollomon, J. H., 1945, "Tensile Deformation," *Trans. Metall. Soc. AIME*, **162**, pp. 268–290.
- [47] ASTM, 2016, "Standard Test Method for Tensile Strain-Hardening Exponents ( $n$ -Values) of Metallic Sheet Materials," ASTM International, West Conshohocken, PA, Standard No. ASTM E646-16.
- [48] Dieter, G. E., 1988, *Mechanical Metallurgy: SI Metric Edition*, McGraw-Hill, London.
- [49] Ludwik, P., 1909, *Elemente Der Technologischen Mechanik*, Springer-Verlag, Berlin, pp. 32–37.
- [50] Namazu, T., and Inoue, S., 2007, "Characterization of Single Crystal Silicon and Electroplated Nickel Films by Uniaxial Tensile Test With in Situ X-ray Diffraction Measurement," *Fatigue Fract. Eng. Mater. Struct.*, **30**(1), pp. 13–20.
- [51] Williams, J. D., 2010, "Fatigue and Fracture Mechanics Aspects of LIGA Fabricated Nickel and Ni-20%Fe Microstructures," *Int. J. Theor. Appl. Multiscale Mech.*, **1**(3), pp. 266–279.
- [52] Lou, J., Allameh, S., Buccheit, T., and Soboyejo, W. O., 2003, "An Investigation of the Effects of Thickness on Mechanical Properties of LIGA Nickel MEMS Structures," *J. Mater. Sci.*, **38**(20), pp. 4129–4135.